Under-ice circulation in an Arctic lake: observations from two field seasons in Lake Kilpisjärvi, Finland

by

Kelly Elise Graves

B.A.Sc., The University of British Columbia, 2011

A THESIS SUBMITTED IN PARTIAL FULFILLMENT OF THE REQUIREMENTS FOR THE DEGREE OF

MASTER OF APPLIED SCIENCE

in

The Faculty of Graduate and Postdoctoral Studies

(Civil Engineering)

THE UNIVERSITY OF BRITISH COLUMBIA

(Vancouver)

April 2015

Abstract

High spatial resolution CTD profiles and Acoustic Doppler Current Profiler velocity measurements show significant rotational basin-wide circulation under ice in May of 2013 and 2014 at Lake Kilpisjärvi, Finland (69°01'N, 20°49'E), a seasonally ice-covered, Arctic lake with negligible through-flow.

In 2013, a high-pressure horizontal density anomaly with vertically paired rotating circulations was observed. The estimated maximum cyclonic and anti-cyclonic azimuthal velocities magnitudes were 0.03 and 0.02 m s^{-1}. The Rossby radius (R_{ri}), the horizontal length scale at which rotational effects become as important as pressure effects, was estimated to be $\sim$ 160 m and the Rossby number (R_0), the ratio of the centripetal acceleration to the Coriolis acceleration, $\sim$ 0.2. It is hypothesized that this circulation was driven by heat flux at the shorelines from warm incoming streams causing a density flow down the slopes to the centre of the lake where the flow converged. This flow was balanced with a shoreward flow beneath the ice. These flows were modified by the earth's rotation which resulted in the rotational circulation observed.

In 2014, a cyclonic, low-pressure horizontal density anomaly was observed near the centre of the lake and was vertically paired with a weak anti-cyclonic anomaly in the top 10 m (mean depth of the lake is 19.5 m).

The estimated azimuthal velocities had maximum cyclonic and anti-cyclonic magnitudes of 0.006 and 0.003 m s^{-1}. The anomaly was estimated to have $R_{ri} \sim 240$ m, with $R_0 \sim 0.12$. It is hypothesized that this circulation was driven by sediment release of heat to the overlying water causing a tilt in the isopycnals near the shores of the lake that caused an inward pressure force that was balanced by the Coriolis force and, to a lesser extent, the centripetal acceleration force.

The 2013 observations were made immediately prior to ice-off, and the 2014 observations were 12 days prior to ice-off. This time difference allowed for significantly different ice and snow conditions, and the addition of warm inflows which forced the circulation closer to the ice-off date. These observations add to the growing understanding of the relationship between thermal distribution and circulation under ice.

Preface

I, Kelly Graves, am the author of this thesis. All work contained in this document is original. I assisted in the design, execution and data collection for both the 2013 and 2014 field seasons at Lake Kilpisjärvi. All analysis is my original work with guidance and supervision from Dr. Bernard Laval.

The 2013 observations at Lake Kilpisjärvi for project *CONCUR*, presented in chapter 2, and the initial analysis, presented in chapter 3 are partially presented in *Axisymmetric circulation driven by marginal heating in ice-covered lakes* by G.B. Kirillin, A.L. Forrest, K. Graves, A. Fischer, C. Engelhardt, and B.E. Laval which has been accepted for publication in Geophysical Research Letters.

Partial observations, presented in chapter 2, and results, presented in chapter 3, from the 2013 field season have been published in *Under-ice, basin-scale circulation in an Arctic Lake* by K. Graves, A.L. Forrest, B.E. Laval, and G. Kirillin which was presented at the Proceedings of the 17th International Workshop on Physical Processes in Natural Waters (Trento, Italy). As well as, *Under-ice circulation, modified by the Earth's rotation, in an Arctic lake* by K. Graves, B. E. Laval, A.L. Forrest, and G. Kirillin which was presented at 22nd International Association of Hydro-Environmental Engineering and Research International Symposium on Ice

(Singapore). Both of these were original works by me.

The 2013 observations that I assisted in collecting have also been presented in *Standing waves during ice breakup in an arctic lake* by G. Kirillin, C. Engelhardt, A. Forrest, K. Graves, B. Laval, M. Leppärant, and W. Rizk which was presented at the Proceedings of the 17th International Workshop on Physical Processes in Natural Waters (Trento, Italy). As well as, *Standing Waves during Ice Breakup in a Polar Lake* by G. Kirillin, C. Engelhardt, A. Forrest, K. Graves, B. Laval, M. Leppärant, and W. Rizk which was presented at 22nd International Association of Hydro-Environmental Engineering and Research International Symposium on Ice (Singapore). A poster, *Polar lake circulation during ice break-up* by G. Kirillin, A. Forrest, K. Graves, and B. Laval was also presented at the European Geoscience Union General Assembly 2014 (Vienna, Austria).

Table of Contents

Abstract ii

Preface iv

Table of Contents vi

List of Figures viii

Acknowledgements x

1 Introduction 1

1.1 Winter Limnology 2

1.2 Observations of Rotational Circulation Patterns in Lakes . . 4

1.3 Rotational Effects on Motion 6

1.3.1 Ekman Number and Thicknesss 8

1.3.2 Rossby Number 9

1.3.3 Geostrophic Flow 10

1.3.4 Cyclogeostrophic Flow 11

1.3.5 Cyclostrophic Flow 13

1.4 Summary 13

2 Methods 14
2.1 Field Site 14
2.2 Field Seasons 16
2.2.1 2013 Field Season 16
2.2.2 2014 Field Season 20
2.3 Data Analysis 22

3 Results 25
3.1 2013 Results 25
3.2 2014 Results 43

4 Discussion 51
4.1 2013 Data Discussion 51
4.2 2014 Data Discussion 55
4.3 2013 and 2014 Comparison 58

5 Conclusion 61

Bibliography 64

Appendices

A Water Sample Results 69

List of Figures

2.1 Map of location of Lake Kilpisjärvi 15

2.2 2013 CTD and ADCP locations 18

2.3 2014 CTD locations 21

3.1 Across and along-lake temperature distributions 26 May 2013 27

3.2 Extents of the 2013 horizontal density anomaly 28

3.3 Direction of the mean ADCP velocities 30

3.4 Across-lake $\partial P \, \partial r^{-1}$, $v_{\theta g}$, and $v_{\theta cg}$ for 26 May 2013 33

3.5 Percent difference for $v_{\theta cg}$ and $v_{\theta g}$ 35

3.6 Contours of the components in the cyclogeostrophic force balance 26 May 2013 36

3.7 Percentage of each component in the cyclogeostrophic force balance 26 May 2013 37

3.8 Contours of patched $v_{\theta cg}$ and percent difference for 26 May 2013 across-lake transect 40

3.9 Along-lake estimates of $v_{\theta g}$ and $v_{\theta cg}$ for 26 May 2013 41

3.10 Comparison of $v_{\theta A}$ to $v_{\theta cg}$ and $v_{\theta g}$ at comparable radial distances 42

3.11 Corrected estimates for $v_{\theta cg}$ with level of no-motion at the bottom for 26 May 2013 44

3.12 Across and along lake temperature distributions 26 May 2014 45

3.13 $\partial P\, \partial r^{-1}$, $v_{\theta g}$, $v_{\theta cg}$, and the percent difference in $v_{\theta g}$ and $v_{\theta cg}$ 48

3.14 Contours of the components in the cyclogeostrophic force balance 26 May 2014 50

Acknowledgements

A few words on a page can not effectively convey the extent of my gratitude for the help and support of many people over the course of my research; however, I will try.

To begin, I must thank the members of the two field teams that I joined at Lake Kilpisjärvi: Georgiy Kirillin, Christof Engelhardt, Alex Forrest, Jeff Williams, Larry Kost, Elisa Lindgren, Tom Kokkonen, Will Rizk, Cecilia Äijälä, and Franzi Pöschke. I will be ever grateful for showing me the ropes (both literally and figuratively). “Kiitos.”

I need to thank both the Environmental Fluid Mechanics and the Physical Oceanography groups at UBC for their input. Also, I greatly appreciate the discussions I had with Greg Lawrence, Roger Pieters, Ted Tedford, Rich Pawlowicz, Stephanie Waterman and Susan Allen.

I also owe great thanks to Andrew Hamilton for his mentorship and daily input.

Also, Bernard Laval, thank you for all of this.

Thanks to my family and friends for putting up with my rambling adventures in the Arctic.

Chapter 1

Introduction

Freshwater lakes cover an estimated 125 000 km^2 (*Wetzel*, 1975) of the earth's surface, and many of these lakes experience ice-cover for some of or a significant portion of their annual lake cycle. However, relatively little is known about their physical dynamics during the ice-cover period. The classic view is there is insignificant circulation (*Welch*, 1952); however, recent observations have shown that ice-covered lakes can experience considerable circulation forced by sediment heat flow, solar radiation, differential heating, seiches caused by the oscillation of the ice-cover, as well as ground and surface water inflows (*Bengtsson*, 1996; *Bengtsson et al.*, 1996; *Kirillin et al.*, 2012). When circulation occurs over large distances or is slow it can be modified by the Coriolis force resulting in rotating density anomalies.

Circulation in ice-covered lakes is important because it transports dissolved and suspended solids, nutrients, and heat throughout a lake body. When circulation patterns persist over time, this has implications for the micro-organisms that live in the lake (*Huttula et al.*, 2010). However, before the effect of under-ice circulation can be understood, the circulation patterns themselves need to be understood (*Rizk et al.*, 2012). This work presents observations made during two winter field seasons at Lake Kilpisjärvi, Finland.

The two field seasons present two markedly different circulation patterns caused by horizontal rotating density anomalies. Before presenting these observations, a review of thermal structure and dynamics of ice-covered lakes is presented.

1.1 Winter Limnology

The thermal structure and dynamics of ice-covered lakes are related, and are markedly different than those that occur during the ice-free period.

The ice-cover period can be broken up into winter 1 and winter 2 (*Kirillin et al.*, 2012). Winter 1 is the the beginning portion of winter when the lake is ice and snow covered. During this time, ice-cover insulates the lake and the heat content of the lake changes very little (*Bengtsson*, 1996) because solar radiation penetration is negligible and has little effect on the heat content of the water column (*Bengtsson et al.*, 1996). This is because most of the incoming solar radiation is reflected off the snow surface and the portion that is not reflected is almost completely absorbed into the snow (*Bengtsson and Svensson*, 1996). Therefore, the thermal structure of the water column is largely determined by atmospheric conditions prior to freeze-up (*Bengtsson and Svensson*, 1996). For example, if wind events were strong prior to ice on, it would take longer for ice to form which would allow the water temperature to cool more (*Wetzel*, 1975). Conversely, weak winds could lead to rapid ice formation and the water would be warmer. Also, the heat content of the lake changes very little because of the low heat conductivity of snow which reduces the transfer heat from the warmer, under-lying water column to the ice and then from the ice through the snow to the atmosphere (*Kirillin et al.*, 2012). The thermal structure beneath the ice-cover is inversely stratified with colder water (0°C at the ice-water interface) overlying warmer water (2°C - 4°C) (*Ellis et al.*, 1991). This occurs in fresh water lakes, where salinity has little to no effect on the density, because density decreases as water temperature decreases below 4°C (the temperature of maximum density).

The main forcing of circulation and mixing in winter 1 is the release of heat from the sediment that accumulated during the summer (*Bengtsson*, 1996; *Zdorovennova*, 2009). This forcing dominates because the ice-cover prevents wind, the predominant driver of circulation during ice-free periods, from transferring momentum to the water surface (*Bengtsson*, 1996). After wind, the next most dominant forcing, through-flow, is reduced during winter because the main precipitation received in the catchments of mid and high latitude lakes is in the form of snow which reduces surface inflows and through-flows.

As winter progresses, the transfer of heat from the sediment to the bottom water decreases (*Bengtsson*, 1996; *Rizk et al.*, 2014). The lake transitions from winter 1 to winter 2 when the water column and the sediment reach the same temperature and no heat is transferred between them (*Kirillin et al.*, 2012). During this time, snow cover begins to disappear and solar radiation is able to penetrate the ice and warm the water column (*Bengtsson*, 1996; *Zdorovennova*, 2009). The amount of solar radiation that reaches the water column is controlled by the amount of remaining snow and the type of ice; more solar radiation penetrates through black ice than white ice which has many air bubbles and scatters more light (*Wetzel*, 1975; *Bengtsson*, 1996). With penetration, the upper water column warms and becomes denser, because the water is below the temperature of maximum density. This causes gravitational instability that drives convection: the main circulation forcing in winter 2.

Near the end of winter 2, the shallower regions around the shores of the lake warm faster than the deeper parts of the lake (*Bengtsson*, 1996) and moats, ice-free regions around the lake (*Vincent and Laybourn-Parry*, 2008), may form. The way in which the ice-surface degrades can affect how the water column warms. If ice degrades evenly, then the water column is warmed consistently over the surface area of the lake. This leads to vertical convection, even mixing of the water column and no horizontal density variability. If the ice surface degrades unevenly, the amount of solar radiation that reaching the water surface varies causing differential heating of the water column. This leads to horizontal density variations across the lake. Horizontal density differences beneath ice-cover have been observed and have, at times, been associated with rotational circulation.

1.2 Observations of Rotational Circulation Patterns in Lakes

Basin-wide rotational circulation patterns, referred to as *gyres*, *eddies* or *vortices*, have been observed in lakes under ice (*Likens and Ragotzkie*, 1966; *Rizk et al.*, 2012; *Forrest et al.*, 2013) and have been predicted by computer simulations (*Huttula et al.*, 2010). Similar circulation patterns have been observed in open-water conditions in lakes; however, open-water horizontal density anomalies are typically forced by wind (*Emery and Csanady*, 1973), seiches interacting with bathymetry (*Kirillin et al.*, 2008), or heat release from bottom sediments (*Akitomo et al.*, 2004). Unlike open-water anomalies, under-ice anomalies are not a result of wind forcings and their smaller differences in density can exist longer because they are not broken up by the wind (*Rizk et al.*, 2012). Radially symmetric, horizontally unstable density anomalies have been observed to persist for a minimum of 6 days (*Forrest et al.*, 2013) to most of the winter (*Rizk et al.*, 2014). Their symmetry implies rotation and the persistence implies that the horizontally unstable density anomalies were held in place by a balance of forces.

Similar rotational circulations have be found under ice in the ocean (*Timmermans et al.*, 2008) and in the atmosphere (*Gill*, 1982). These types of flow are common in dynamic meteorology; therefore, most dynamic meteorology texts include sections on these flows that detail their characteristics and the methods used to analyze them. There does not exist a physical limnology reference that summarizes rotational circulations in lakes using similar methods. This work makes an attempt to fill that gap. To be able to do that, first a summary of relevant geophysical fluid flows and characterizations methods are presented. These methods are then used to analyze the under-ice observations made at Lake Kilpisjärvi, Finland in 2013 and 2014. Finally, results are compared to previous observations of rotating horizontal density anomalies.

1.3 Rotational Effects on Motion

Rotating circulation under ice is often associated with density differences. It is not always clear whether the circulation is caused by the density differences, or if the density differences are caused by the rotating circulation. The density stratification in these flows results in barotropic pressure forces and maintains circulation (*Holton*, 2004). Most often, these flows occur over large length scales, such as oceanic and atmospheric currents; however, there are similar small scale flows in the environment, such as those observed in some lakes. These flows are affected by the earth's rotation because of their long time scale.

For flows that are not affected by the earth's rotation, the coordinate system used for analysis is fixed with reference to the distance stars, and a rotating coordinate system that rotates with the earth is used. To a stationary observer of these flows on Earth, the flow is deflected by an "apparent force", (i.e. that does no work), referred to as the Coriolis force, which is a result of the earth's rotation (*Stommel and Moore*, 1989; *Kundu and Cohen*, 2004). For these types of flows, positions and motions are referenced to a fixed point on the earth which rotates at a constant rate about the poles ($\Omega = 2\pi$ rad day^{-1} where Ω is angular velocity) with respect to the inertial frame. The intensity of the rotation varies with latitude (θ) and is given by $f = 2\Omega sin\theta$ where f is the Coriolis parameter.

To determine whether a motion is significantly affected by the Coriolis force, the horizontal length scale of the motion is compared to the Rossby radius of deformation given by

$$R_r = \frac{c}{f} \tag{1.1}$$

where c is the wave speed. R_r is the horizontal length scale at which rotational effects become as important as pressure effects. When the length scale of the motion of interest is much less than R_r, the motion is not affected by the earth's rotation. When the horizontal length scale is comparable to or greater than R_r, then the earth's rotation is important. R_r can either be external (R_{re}) or internal (R_{ri}). R_{re} is a comparison of the barotropic pressure to the Coriolis forces, and uses the shallow water, non-dispersive wave speed given by $c = \sqrt{gh}$ where g is gravitational acceleration, and h is the depth of the fluid of interest. R_{ri} is a comparison of the baroclinic pressure to the Coriolis forces. It is an approximation of a two-layer system, with $c = \sqrt{g' h_{eq}}$ where $g' = g\frac{\Delta\rho}{\rho_0}$ is the reduced gravity (ρ_0 is the reference density of 1000 kg m^{-3}) and h_{eq} is an adjusted layer thickness.

For lake circulation to be influenced by the Coriolis force, the lateral lake dimensions must be equal to or greater than R_r (*Gill*, 1982; *Rizk et al.*, 2014). R_{ri} is smaller than R_{re}, and for ice-covered lakes, is typically around a few hundred meters, which is generally smaller than the lateral dimensions of the lake; therefore, the Coriolis force can play an important role in lake motions under ice-cover (*Rizk et al.*, 2014).

These rotational circulations can be idealized to be steady state (independent of time) and purely horizontal (vertical motion is negligible compared to horizontal motion); therefore, the residual accelerations ($du\ dt^{-1}$,

$dv\ dt^{-1}$, $dw\ dt^{-1}$) are equal to zero (*Gordon et al.*, 1998). To simplify the analysis of these flows, the frictional effects, away from the boundaries, need to be estimated and found to be negligible.

1.3.1 Ekman Number and Thicknesss

Frictional effects are estimated with the Ekman number, the ratio of the viscous force to the Coriolis force (per unit volume) (*Kundu and Cohen*, 2004), which is given by

$$E = \frac{\text{viscous force}}{\text{Coriolis force}} = \frac{\nu}{fL^2} \tag{1.2}$$

where ν is the kinematic viscosity which has a molecular value of 10^{-6} m^2 s^{-1} and has been observed under ice to be 10^{-4} m^2 s^{-1} (*Bengtsson*, 1996), and L is the horizontal length scale of the flow. When E <<1, frictional effects are negligible. This is the case for most flows away from boundaries (*Greenspan*, 1968). The distance from the boundary where friction becomes important is given by the Ekman boundary layer thickness given by

$$\delta_{Ek} = \sqrt{\frac{2A_v}{f}} \tag{1.3}$$

(*Kundu and Cohen*, 2004) where A_v is the vertical turbulent viscosity coefficient which has been estimated to have a maximum value under ice of ∼ 10^{-4} m^2 s^{-1} (*Bengtsson*, 1986). Varying f from 0 to 1.45 x 10^{-4} s^{-1} (maximum occurs at the poles), and using the maximum value for the turbulent eddy viscosity, δ_{Ek} ranges from 0 to 1.4 m. Above this distance from the bottom, frictional effects can be neglected.

The viscosities in (1.2) and (1.3) are different, and their values vary depending on the reference. (*Pedlosky*, 1987) (1987) replaced A_v by ν for laminar flow. For conservative estimates, values that give the largest E and δ_{Ek} can be used. Or, a range of viscosities from molecular to the maximum turbulent eddy viscosity can be used.

Once frictional effects are estimated to be negligible, common steady, rotational circulations can be analyzed. These types of circulations are defined by the forces that contribute to their balances. They are: (1) geostrophic (i.e. between Coriolis and pressure forces), (2) cyclogeostrophic (i.e. between Coriolis, centripetal acceleration, and pressure forces), and (3) cyclostrophic (i.e. between pressure and centripetal acceleration forces).

1.3.2 Rossby Number

One way to estimate whether a system is in geostrophic or cyclogeostrophic balance is to calculate the Rossby number (R_o). This is the ratio of the centripetal acceleration to the Coriolis acceleration, and is an estimate of the importance of non-linear terms (convective acceleration) (*Greenspan*, 1968). R_o is given by

$$R_o = \frac{\text{non-linear acceleration}}{\text{Coriolis acceleration}} \approx \frac{U^2/L}{fU} = \frac{U}{fL} \approx \sqrt{\frac{g'H}{f^2L^2}} = \frac{R_{ri}}{L} \tag{1.4}$$

where U and L are the horizontal velocity and length scales. For geostrophic flow, the Coriolis force is much more important, so R_o <<1, for cyclogeostrophic flow R_o is $O(1)$, and for cyclostrophic flow R_o >>1.

1.3.3 Geostrophic Flow

Geostrophic flow occurs when a pressure gradient force is balanced by the Coriolis force (R_o <<1). This type of balance is not valid near the equator (because f becomes small), near boundaries (so, E <<1) or for unsteady flows (*Kundu and Cohen*, 2004). The flow from high to low pressure is modified, or deflected by the earth's rotation. In the northern hemisphere, the deflection is to the right of the pressure force and to the left in the southern hemisphere. This causes the flow to be along lines of constant pressure or density (isobars) (*Cushman-Roisin*, 1994). The horizontal force balances per unit mass are given by

$$fu_g = -\frac{1}{\rho_0}\frac{\partial P}{\partial y} \tag{1.5}$$

$$fv_g = +\frac{1}{\rho_0}\frac{\partial P}{\partial x} \tag{1.6}$$

where u_g and v_g are the geostrophically balanced velocities in the x and y directions respectively, and P is pressure. If the pressure distribution is known, the horizontal velocities are given by

$$u_g = -\frac{1}{\rho_0 f}\frac{\partial P}{\partial y} \tag{1.7}$$

$$v_g = \frac{1}{\rho_0 f}\frac{\partial P}{\partial x} \tag{1.8}$$

and referred to as the *geostrophic wind* (*Gill*, 1982). Since geostrophic circulation is rotational, cylindrical co-ordinates (r, θ, z) can be more useful than Cartesian co-ordinates. The equivalent horizontal velocity in cylindrical coordinates is the azimuthal geostrophic velocity ($v_{\theta g}$) and is given by

$$v_{\theta g} = \frac{1}{\rho_0 f}\frac{\partial P}{\partial r} \tag{1.9}$$

where r is the radial distance from the centre of the rotation.

If the hydrostatic assumption is made, given by

$$\frac{\partial P}{\partial z} = -\rho g \tag{1.10}$$

(*Kundu and Cohen*, 2004), and is combined with (1.7) and (1.8), the vertical shear of the horizontal velocity is related to the horizontal density gradients. This shows that the Coriolis force allows a horizontally unstable system, where pressure/density varies horizontally, to be maintained without any input of additional energy (*Cushman-Roisin*, 1994). This is known as *thermal wind* in atmospheric science.

1.3.4 Cyclogeostrophic Flow

Cyclogeostrophic flow, away from boundaries ($E <<1$), occurs when there is a balance between pressure gradient, Coriolis, and centripetal acceleration forces. Since the centripetal acceleration and Coriolis forces are of comparable magnitude, R_o $O(1)$. In the force balance, which is also referred to as a *gradient wind balance*, the centripetal acceleration force is always directed outwards from the centre of the horizontal pressure anomaly. The direction of the pressure force depends on whether the system is high or low pressure; the resultant pressure force from a high-pressure anomaly points outwards, and vice versa for a low-pressure anomaly. The direction of the

Coriolis force then balances the pressure and centripetal acceleration forces. The resulting velocity is directed is to the right of the pressure force (in the northern hemisphere).

The cyclogeostrophic force balance per unit mass is given by

$$-\frac{v_{\theta cg}^2}{r} - f v_{\theta gc} = -\frac{1}{\rho_0}\frac{\partial P}{\partial r} \tag{1.11}$$

where, from left to right, the terms are the centripetal acceleration, Coriolis and pressure forces per unit mass, and $v_{\theta cg}$ is the cyclogeostrophic azimuthal velocity. (1.11) can be solved for $v_{\theta cg}$ using the quadratic formula. This gives two solutions for $v_{\theta cg}$ from

$$v_{\theta cg} = -\frac{fr}{2} \pm \sqrt{\frac{(fr)^2}{4} + \frac{r}{\rho_0}\frac{\partial P}{\partial r}}. \tag{1.12}$$

To determine which solution is correct, it is important to remember that cyclogeostrophic flow is a result of the pressure gradient, and, if there is no pressure gradient, there is no flow. The solution of interest from (1.12) is the positive root (as the negative root will give a value for $v_{\theta cg}$ even if there is no pressure gradient). The direction of the flow depends on the type of pressure system. In the northern hemisphere, flow is cyclonic (in the same direction as the earth's rotation) for a low-pressure centre (low-density) and anti-cyclonic for a high-pressure centre (high-density) (*Gill*, 1982).

It is possible for the radicand (the terms under the square root) in (1.12) to be less than zero. This results in a complex solution for the azimuthal velocity, which indicates the system is no longer in cyclogeostrophic balance due to two possibilities. (1) There is acceleration across isobars and the system is unsteady or affected by friction. (2) The radius of curvature is too small to balance the horizontal pressure difference.

1.3.5 Cyclostrophic Flow

Cyclostrophic flow occurs when the Coriolis force can be neglected; therefore, there is a force balance between the centripetal and pressure gradient forces, given by

$$\frac{v^2}{r} = \frac{1}{\rho_0}\frac{\partial P}{\partial r} \tag{1.13}$$

which results in cyclostrophic motion. This occurs when the horizontal scales are small, or f is small. This type of system only exists for a low-pressure anomaly because it balances the outward oriented centripetal force (*Cushman-Roisin*, 1994). This is the type of balance that allows dust devils and waterspouts to exist (*Renno and Bluestein*, 2001). The flow is normal to the direction of the balance. Cyclostrophic flow can be cyclonic or anti-cyclonic. For cyclostrophic flow, $R_o >>1$ because the centripetal acceleration is much more important than the Coriolis acceleration.

1.4 Summary

For ice-covered lakes in winter 2, the increased solar radiation penetrating through the degrading snow and ice cover can lead to horizontal density differences. These density difference cause horizontal pressure gradients that can exist in geostrophic, cyclogeostrophic or cyclostrophic balance. For these balances to exist, there must be rotational circulation.

Chapter 2

Methods

This chapter first presents geographical, environmental and weather information on the field site studied, Lake Kilpisjärvi, Finland. Then the data collected and the collection methods used during the two field seasons are presented. Finally, the methods used to analyze the data are described.

2.1 Field Site

Lake Kilpisjärvi is a seasonally ice-covered lake located in northwestern Finland at 69°01N, 20°49E (Figure 2.1). Since it is above the Arctic Circle, it is referred to as an arctic or polar lake. It is below the tundra line, the 10°C July isotherm, and the Arctic marine boundary (*Vincent and Laybourn-Parry*, 2008). The shores of the lake are bordered by Finland (east, north-east and south), Sweden (west), and Norway (north-west). Lake Kilpisjärvi has two basins: the north basin and the south basin. This study focuses on the north basin, which has a mean depth of 19.5 meters (m) (*Leppäranta et al.*, 2012), a maximum depth of 57 m, a surface area of 37.2 square kilometres (km^2) and is located 473 m above sea level (*Yang et al.*, 2013). The major inflow is from Lake Siilasjärvi in the north. There are numerous smaller surface inflows from streams from the low-lying mountains that sur-

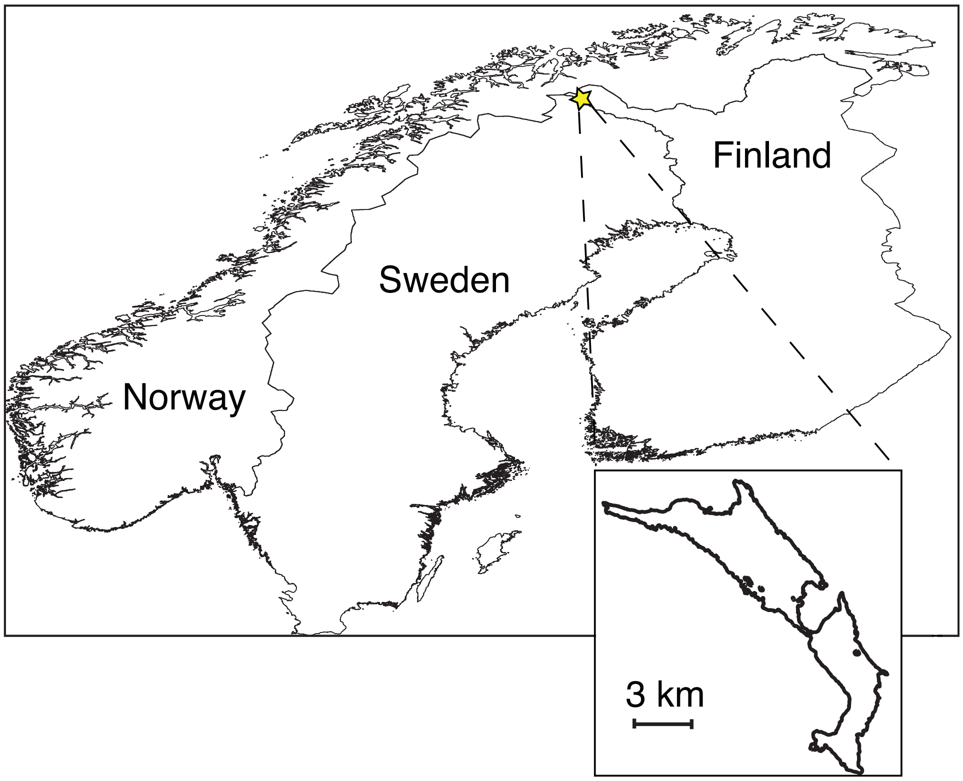

Figure 2.1: Map of Finland, Sweden and Norway. The yellow star is the location of Lake Kilpisjärvi which is shown in the inset.

round the shore of Lake Kilpisjärvi. During spring, snowmelt flows overland into the lake. The north basin of Lake Kilpisjärvi flows into the south basin which then flows into the River Könkämäeno and then eventually into the Baltic Sea.

The climate can be characterized as sub-arctic. Records from the Kilpisjärvi Biological Station (run by the Faculty of Biological and Environmental sciences at the University of Helsinki) located on the east shore of the lake show the annual mean average air temperature is -2.3°C, with a mean annual wind-speed of 2.52 m s^{-1} and a total annual precipitation is 447 mm in the form of snow and rain. The mean date of ice break-up/ice-off is 18 June, the latest break-up was 1 July 1997 and the earliest was 2 June 1963. In this case, ice break-up and ice-off both refer to when the majority of the lake is free of ice.

2.2 Field Seasons

Two field campaigns were conducted at Lake Kilpisjärvi from 25 May to 3 June 2013 and 19 May to 26 May 2014.

2.2.1 2013 Field Season

The first field campaign was for the project named *Solar convection and lateral currents under lake ice cover* (CONCUR), which took place at Lake Kilpisjärvi from 25 May to 3 June 2013. This field campaign was part of an international collaboration with Germany, Finland, and Canada. Funding for the project was provided by the International Network for Terrestrial Research and Monitoring in the Arctic (INTERACT) and Natural Sciences and Engineering Research Council of Canada (NSERC).

At the beginning of the field campaign, the lake was covered with 0.6 m of ice with the exception of the shallow areas around the shores of the lake (littoral areas) that were free of ice cover and became larger with time. These areas shall be referred to as moats (*Vincent and Laybourn-Parry*, 2008). The ice itself was made up of regions of solid ice, and regions of candlestick ice (vertical columns of ice that are tightly packed together). There was no snow on the ice-surface and very little snow on the shores.

During this period of time, there was 24 hours of daylight.

From 26 May onwards, Lake Kilpisjärvi was subject to rapidly warming temperatures. After 27 May, the ice surface was unsafe to work on because it began to degrade and break-up. On 6 June 2013 Lake Kilpisjärvi experienced the earliest ice-off since 1963.

Data Collected

Conductivity-temperature-depth (CTD) loggers, made by Richard Brancker Research Ltd. (RBR) XR-620, were used to collect measurements of temperature and conductivity vertically through the water column (profiles). The RBR CTD was set to start collecting measurements when it reached a certain pressure value (pressure thresholding). The RBR CTD recorded 6 samples per second (i.e. 6 Hz) and the CTD was lowered at approximately 0.5 m s^{-1}. The RBR CTD has a conductivity range of 0 to 2 mS cm^{-1}, a resolution <0.00002 mS cm^{-1} and an accuracy of ± 0.003 mS cm^{-1}. The temperature ranges from -5 to 35°C, has a resolution of <0.002°C and an accuracy of ± 0.002°C. The pressure has a resolution of <0.001 %, and an accuracy of ± 0.05 %.

To collect measurements under the ice-surface, holes were drilled through the ice with a hand-auger. Ice chunks and slush were removed from the holes and the CTD was lowered down through the water column by hand until it reached the bottom then it was raised. When the holes were initially drilled, ice thickness and snow depth measurements were collected at each CTD profile location. To measure the thickness of the ice, a fishing gaff (a pole with a hook on the end) was lowered through the hole in the ice until it caught on the under side of the ice and the location of the water surface was noted on the fishing gaff. Snow depth was measured with a ruler in the ice hole where it was easier to note the transition from ice to snow.

The CTD profiles were used to construct transects which are a series of vertical profiles that are evenly spaced along a straight line. Two CTD transects were establish during this field campaign: across-lake, and along-lake transects. These are shown on Figure 2.2.

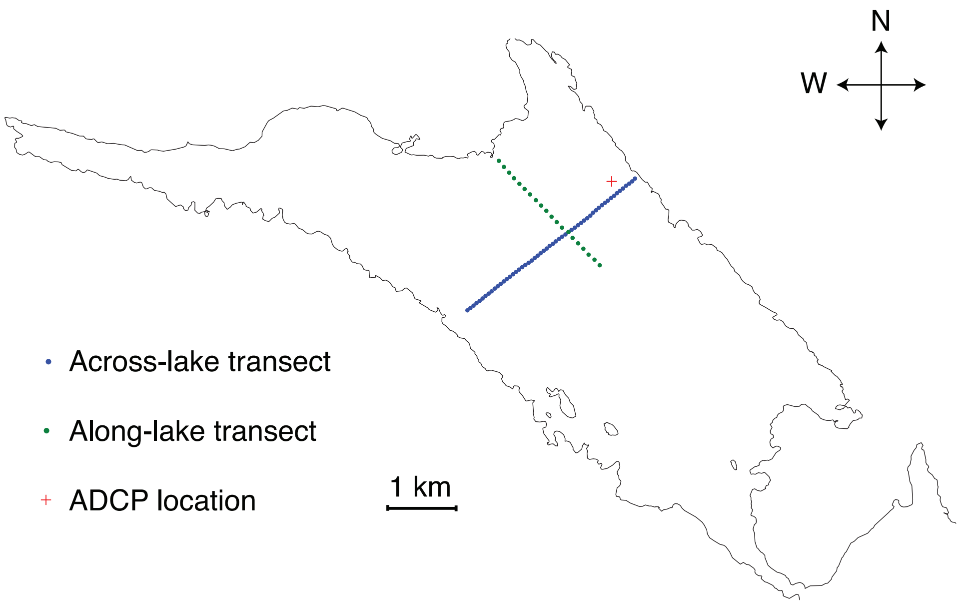

Figure 2.2: 2013 CTD profile locations for the across-lake transect (blue circles) and along-lake transect (green circles), and the ADCP location (red dot). This map only shows the north basin of Lake Kilpisjärvi.

The across-lake transect consisted of profiles spaced approximately 50 m apart starting 50 m from the eastern shore and reaching to approximately 100 m from the western shore. On the morning of 25 May, the first 16 profiles of the across-lake transect were collected. In the evening of 25 May, the same 16 CTD profiles were repeated and 9 more profiles were added to the western most profile for a total of 25 profiles. On 26 May, the 25 profiles were repeated and 31 new profiles were added across the width of the lake starting at the western most profile for a total of 56 profiles.

The along-lake transect consisted of 20 profiles spaced approximately 100 m apart starting from approximately 100 m from the northern shore. This transect was collected at the same time as the full across-lake transect on 26 May. The two transects intersected at profile 14 of the along-lake transect and profile 23 of the across-lake transect. These transects were collected over a period of three hours and can be considered synoptic.

After the CTD transects were collected, a 600 kHz Teledyne RD Instruments Acoustic Doppler Current Profiler (ADCP) was used to collect velocity measurement profiles in the water column at one location that can be seen in Figure 2.2. The ADCP collected measurements every 5 seconds from 23:07:39 30 May 2013 to 15:07:39 4 June 2013. The ADCP was mounted on the bottom of the lake at 18.65 m with the beams looking upwards. It recorded northern and eastern velocities in 65 vertical bins that are 0.3 m tall. The measurements begin 1.72 m from the bottom and reach 20.92 m above the bottom (the bins near the surface were removed as they partially extended above surface).

Air temperature, snow depth and rain data was provided by the Kilpisjärvi Biological Station for April, May, June and July of 2013. Hourly averages of wind speed and direction for May and June 2013 were provided by the Finnish Meteorological Institute.

Three water samples were collected on 2 June 2013 and a laboratory analysis was conducted to determine the chemical composition of the lake water. The results of the chemical analysis can be found in Appendix *A*. The chemical composition was used to determine the water density.

2.2.2 2014 Field Season

The second field campaign was for the project named (LACUNA) which took place at Lake Kilpisjärvi from 19 May to 26 May 2014. The project was partially funded by INTERACT, NSERC and Northern Scientific Training Program (NSTP). It was an international collaboration between Germany, Finland, Australia, and Canada. The objective of this project was to investigate, through another intensive field campaign, how under-ice circulation observed in spring forms and collapses.

During the winter leading up to the campaign, Lake Kilpisjärvi was subject to record snowfall. Some of this snow and slush was still present on the ice throughout the campaign. At the beginning of the campaign, the ice was 1 m thick. No additional snow accumulated and no moats formed around the exterior of the lake during the campaign. There was 24 hours of sunlight for the duration of the field campaign. Some icy rain fell during the field campaign; however, not significant amounts.

Data Collected

Two JFE Advantech CO., Ltd. RINKO CTD profilers collected measurements of temperature and conductivity through the water column. The RINKO CTD profilers were set to start collecting data when the external switch was turned on prior to being lowered through the auger hole in the ice at approximately 0.5 m s^{-1}. The RINKO CTD profiler has a conductivity range of 2 to 70 μS cm^{-1}, a resolution of 0.001 μS cm^{-1} and an accuracy of $\pm$ 0.01 μS cm^{-1}. The temperature sensor has a range of -3 to 45°C, resolution of 0.001°C, and an accuracy of $\pm$ 0.001°C. The depth range is 0 to 600 m, resolution of 0.01 m, and an accuracy of $\pm$ 0.3 %.

The locations of the CTD profiles were chosen to repeat some of the CTD profiles from the previous field season. The across-lake transect consisted of 29 profiles spaced at 100 m intervals (instead of intervals of 50 m from the 2013 field season). The along-lake transect was shifted to the approximate centre of across-lake transect and consisted of 10 profiles spaced at 100 m intervals. The across and along-lake profile locations can be seen on Figure 2.3.

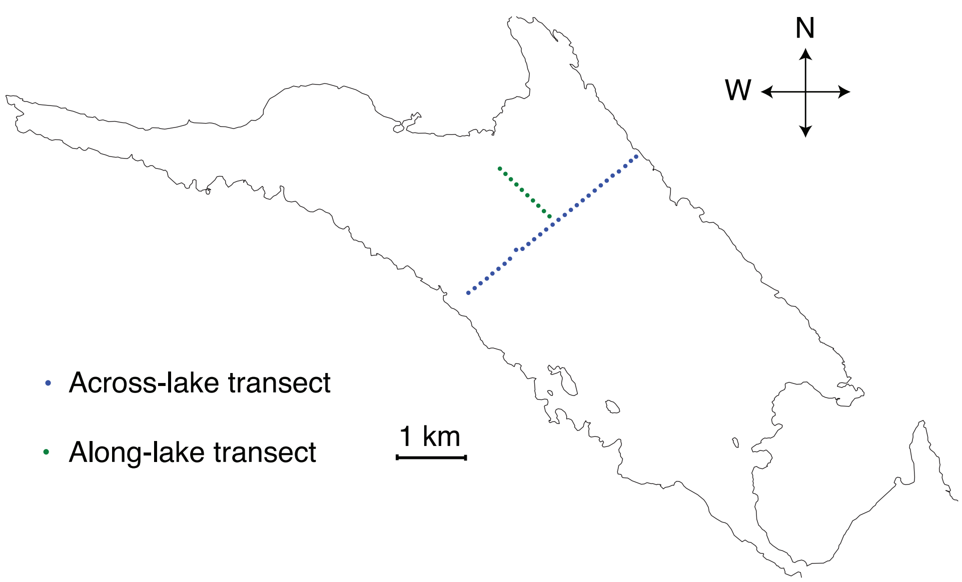

Figure 2.3: 2014 CTD profile locations for the across-lake transect (blue circles) and along-lake transect (green circles). This map only shows the north basin of Lake Kilpisjärvi.

On 19 May 2014, 9 CTD profiles were collected with a RINKO CTD logger on the across-lake transect. On 20 May 2014, CTD profiles were collected at the previous 9 CTD locations and 20 more profiles were collected (total transect of 29 profiles). The same 29 profiles were repeated on 21 May, in reverse order. The along-lake transect also collected on 21 May. This transect started between profile 14 and 15 on the across-lake transect. Both across and along-lake transects were repeated on 22 May. On 23 and 24 May, the across-lake transect was repeated. On 26 May, both the across and along lake transects were repeated.

Air temperature, snow depth, and rain data was provided by the Kilpisjärvi Biological Station for April, May, June, and July of 2014. Hourly averages of wind speed and direction for May and June 2014 were provided by the Finnish Meteorological Institute.

2.3 Data Analysis

The purpose of the analysis of the CTD measurements is to investigate basin-scale temperature and density patterns. To remove small-scale variability, the CTD profiles were vertically averaged every 1 m, the top 1 m of data was removed to reduce variability, and the profiles were horizontally averaged every 100 m. The location of the data points is recorded in latitudes, longitudes, and depths below the water surface.

The measured temperatures, conductivities and water composition give the density of the water at each data point calculated using the International Thermodynamic Equation of Seawater (TEOS-10) (*McDougall and Barker*, 2011). The density distribution was analyzed to characterize horizontal density anomalies.

The internal Rossby radius of deformation (R_{ri}) and the Rossby number (R_o) were calculated to determine whether the system was in geostrophic or cyclogeostrophic balance. For this calculation, the difference in density between the horizontal density anomaly core, and the surrounding water was determined. The mean density of the core was calculated for the region of water encapsulated within the horizontal and vertical extents of the anomaly. The mean density was calculated for the surrounding regions. The density difference, the height of the horizontal density anomaly, and the Coriolis parameter (f) were used to calculate R_{ri}. When this radius is the same order of magnitude as the observed radius of the horizontal density anomaly, the water (away from boundaries) is assumed to be in cyclogeostrophic balance.

To confirm that the friction effects were minimal, the Ekman number (E) (1.2) and the Ekman thickness (δ_{Ek}) (1.3) were calculated, both assuming that the vertical turbulent viscosity coefficient is $\sim 10^{-4}$ m^2 s^{-1} (*Bengtsson*, 1986) and the kinematic viscosity is $\sim 10^{-6}$ m^2 s^{-1}. These values were chosen because they will give the maximum values of E and δ_{Ek} which is conservative.

Making the hydrostatic assumption (1.10), and assuming that the horizontal pressure difference is zero at the surface (equivalent to assuming a level of no-motion at the surface), the azimuthal cyclogeostrophic velocities ($v_{\theta cg}$) were estimated from (1.12). The hydrostatic pressure field was determined by $P = \int_z^0 \rho g dz \sim \sum_1^n \rho_n g \partial z$ where ρ_n is the density of a given water parcel, g is the gravitational acceleration (9.81 m s^{-2}) and z is the height of the water parcel. The horizontal pressure gradient ($\partial P \partial r^{-1}$) is approximated between neighbouring profiles (∂P) over the distance separating them (∂r) when the core of the density anomaly lies along the current transect. If the transect that is being analyzed does not cross through the centre of horizontal density anomaly, then the horizontal pressure differences are calculated between the transect profiles and the assumed centre of the horizontal density anomaly. The calculated horizontal pressure gradient is evaluated halfway between the profiles for which the difference is calculated. For a dense-core (high-pressure) horizontal density anomaly, the positive root solution (1.12) is used to calculate $v_{\theta cg}$. For dense-core anomalies, certain values of $\partial P\, \partial r^{-1}$ and r near the centre have no real and physical solution (section 1.3.4). To find a solution for this region, the azimuthal geostrophic velocities ($v_{\theta g}$) from (1.9) are used if they are found to be of the same order as $v_{\theta cg}$.

The magnitudes of the ADCP velocities in the azimuthal direction ($v_{\theta A}$) were compared to the estimated azimuthal velocities ($v_{\theta cg}$ and $v_{\theta g}$) obtained from the CTD measurements.

Chapter 3

Results

This chapter presents the results of the analysis of the data collected in the 2013 and 2014 field campaigns at Lake Kilpisjärvi.

3.1 2013 Results

The ice had a mean thickness of 0.6 m at the beginning of the field campaign (25 May 2013) and 0.4 m immediately prior to break-up on 3 June 2013. There was no snow on the ice for the duration of the campaign. The daily mean air temperature increased from 5.9°C on 25 May 2013 to 10.4°C on 3 June 2013, and the mean air temperature for the period of study was 11.7°C (calculated using the daily mean air temperatures). The wind had a mean speed of 10 km hr^{-1} and a mean direction of 184°. For Lake Kilpisjärvi, the water temperatures ranged between 0 and 3.1°C, and the specific conductance ranged from 15.7 to 20.2 μS cm^{-1}. For a lake with this range of water temperatures and specific conductance, the temperature has a greater effect on the density than the specific conductance; therefore, the temperature and density distributions follow the same pattern, and density increases with increasing temperature.

From the distributions of water temperature on the across and along-lake CTD transects on 26 May 2013 (Figure 3.1), it can be seen that the water temperature increases with depth which is expected for an ice-covered lake (the water is inversely stratified). Horizontally, the water temperature is not uniform. For most of the water column, the temperature decreases horizontally away from the shore, and then increases again near the centre of the lake. This horizontal temperature variation indicates that the water is horizontally unstable. It is considered horizontally unstable because there is colder, less dense water beside warmer, denser water, which implies a horizontal pressure gradient. The temperature transects also show that within 10 m of the bottom boundary, isotherms run parallel to the slope of the boundary. This indicates a flow parallel to the bottom slope directed towards the centre of the lake. The across-lake CTD transect shows that there is a region of warmer, denser water near the centre of the lake that is nearly cylindrical and is surrounded by cooler, less dense water. This creates a horizontal density difference between the inner, dense core and the surrounding less dense water. In atmospheric and oceanic sciences, this is referred to as a dense-core/high-pressure horizontal temperature (or density) anomaly. The across-lake CTD transect is a vertical slice through this structure.

From visual inspection, the cylindrical core of the anomaly is located on the across-lake transect approximately 1600 m from the east shore with an approximate radius of 350 m and a height of 22 m. The along-lake transect did not intersect the across-lake transect near the core of the density anomaly, which is why the core of denser water does not appear on the along-lake transect.

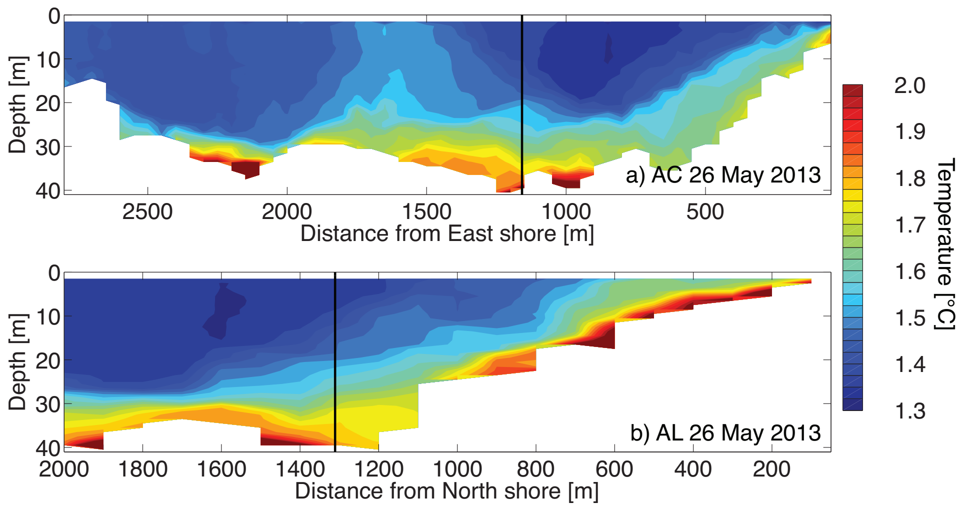

Figure 3.1: Contour plots of temperature with contours every 0.025°C ranging from 1.3 to 2.0°C. The across and along-lake transects are shown in panel a) and b) respectively. The data has been vertically averaged every 1 m. The distance along the x-axis is the distance from the eastern and northern shores for panels a) and b) respectively. The black vertical lines represent the location where the two transects intersect at 90°.

The density distribution, which has the same pattern as the temperature distribution, is used to investigate the force balance of the horizontal density anomaly and the surrounding water. The centre of the horizontal density anomaly was determined to be 1600 m from the east shore by calculating the location about which the anomaly is symmetric and the location of the least horizontal density variability. Since the anomaly is not perfectly symmetric, both the eastern and western anomaly radii on the across-lake transect were estimated to determine the width of the anomaly. The anomaly radii are the locations where the horizontal density difference is the greatest (i.e. where the anomaly transitions to the surrounding water) in Figure 3.2. The eastern and western maximum radial distances are estimated to be approximately

370 m and 320 m. The radius is taken to be 350 m. The height of the anomaly was taken as the vertical distance in the water column that has the greatest density difference, which is 22 m.

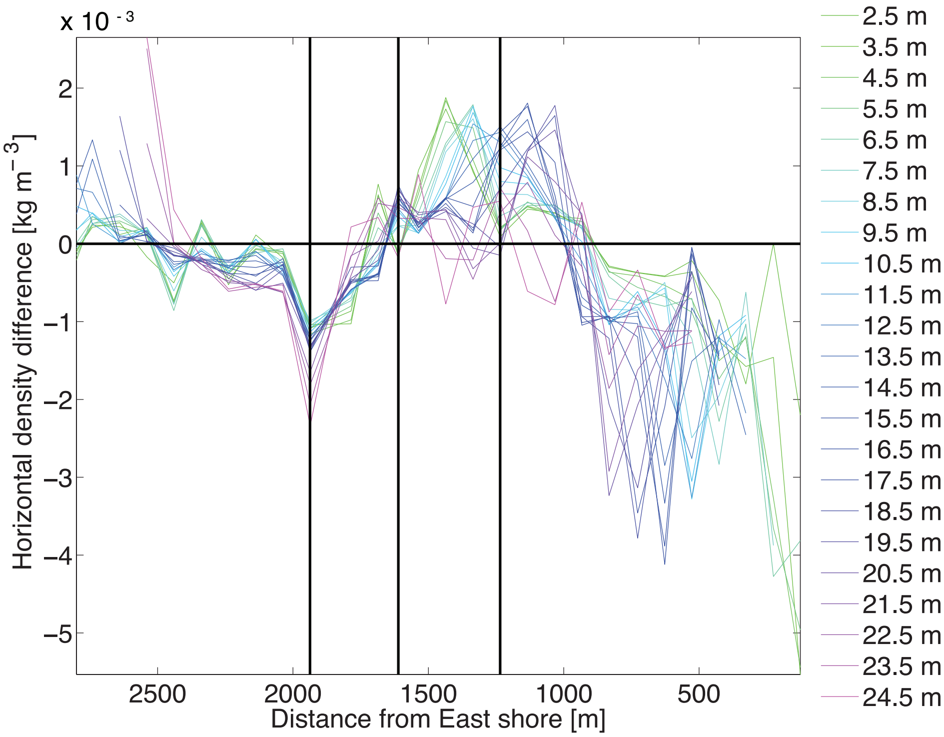

Figure 3.2: Horizontal density differences [kg m^{-3}] for depths ranging from 2.5 to 24.5 m. The distance along the x-axis is the distance from the eastern shore. The region of interest falls between 1000 and 2000 m. The left and right-most vertical lines represent the western and eastern horizontal extents of the density anomaly. The centre vertical line represents the vertical axis about which the horizontal density anomaly is symmetric (the centre).

Considering that the horizontal density anomaly is approximately radially symmetric about the centre, a cylindrical coordinate system (r, θ and z) is used for the analysis where r is the radial distance from the centre of the horizontal density anomaly, θ is taken to be positive counter-clockwise,

$0°$ to the east and $180°$ to the west on the across-lake, and z is the vertical distance taken as positive downwards.

Since the inner core is assumed to be steady and is denser than the surrounding water, the core is applying an outward pressure force on the less dense water; therefore, there must be a force directed towards the centre of the anomaly that is balancing the outward pressure force. If the anomaly was not affected by the Coriolis force, the inner water would flow radially outwards and the outer water would flow inward over top of the denser water until the system reached equilibrium. However, this was not observed which suggests a balance that includes Coriolis force.

To estimate whether the balance was affected by the earth's rotation, the internal Rossby radius, R_{ri}, was estimated by first determining the density difference between the dense core of the horizontal density anomaly (mean density of 999.9603 kg m^{-3}) and the surrounding less dense water (mean density of 999.9579 kg m^{-3}). The mean density difference between the core and surrounding water was 0.0024 kg m^{-3} which gives an effective gravity of 2.2 x 10^{-5} m s^{-2}. When the estimated height of the anomaly, 22 m, and f of 1.36 x 10^{-4} s^{-1} (for a latitude of 69°) are used, $R_{ri} \sim 160$ m. This is less than the observed radius of 350 m, indicating the anomaly was modified by the earth's rotation and was in either geostrophic or cyclogeostrophic balance. Cyclostrophic balances do not exist for dense core anomalies (section 1.3.5); therefore, it is not in cyclostrophic balance. Because this is a dense-core anomaly in the northern hemisphere, with a level of no-motion assumed at the surface, the circulation is anti-cyclonic (clockwise) about the centre of the anomaly. The direction of the measured ADCP velocities support the prediction of anti-cyclonic circulation. The direction of the mean ADCP velocities can be seen in Figure 3.3.

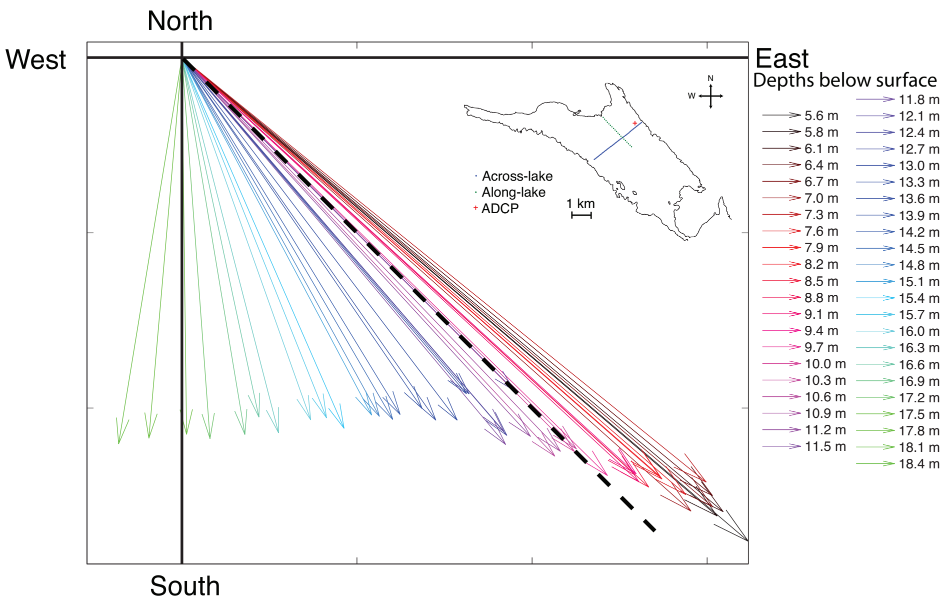

Figure 3.3: Direction of the mean ADCP velocities over the depth of the water column (shown with varying colours and the line lengths are proportional to the mean velocity). The dashed line is the azimuthal direction. The inset map is of the ADCP location (red cross) with respect to the CTD transects.

The high density core, the direction of the ADCP velocities, and R_{ri} support a rotational circulation in a balance modified by the earth's rotation. This balance is either geostrophic or cyclogeostrophic. Using R_{ri} and L $\sim$ 350 m, R_o (1.4) $\sim$ 0.2. This indicates magnitude of the centripetal acceleration force is approximately 20 % of the magnitude of the Coriolis acceleration force. This does not automatically indicate whether the anomaly is in geostrophic (R_o <<1) or cyclogeostropic (R_o $O(1)$) balance; therefore, further analysis is needed of both balances to determine which is most appropriate.

To investigate the geostrophic and cyclogeostrophic balances using the methods discussed in section 2.3, friction needs to be neglected. To confirm that this is reasonable, the Ekman number (1.2) was estimated for a range of eddy viscosities 10^{-6} m^2 s^{-1} (molecular) (*Bengtsson et al.*, 1996) to 10^{-4} m^2 s^{-1} (turbulent) (*Bengtsson*, 1996) with L $\sim R_{ri}$. E ranged from $\sim 10^{-10}$ to 10^{-8} which are both <<1; therefore, frictional effects can be neglected. The Ekman boundary layer thickness (1.3) was found to range from 0.1 to 1.2 m (for molecular and turbulent viscosity). To be conservative, $\delta_{Ek} \sim 1.2$ m and the balances are valid above this distance from the bottom boundary.

To estimate the azimuthal velocity distribution for both the geostrophic and cyclogeostrophic balances, the horizontal pressure gradient distribution ($\partial P \; \partial r^{-1}$) is needed. It is determined by assuming that the ice surface has zero horizontal pressure variability which is equivalent to assuming that there is no motion at the surface. This assumption has been used by *Forrest et al.* (2013) and is a good first estimate for use in ice-covered lakes. The horizontal pressure difference is calculated outwards from the centre of the horizontal density anomaly; therefore, a negative horizontal pressure difference corresponds to decreasing pressure with increasing radial distance, and a positive value has increasing pressure with increasing radial distance. $\partial P \; \partial r^{-1}$ for the 26 May 2013 across-lake transect is shown in Figure 3.4 a. Near the centre of the transect, within a radial distance of 750 m from the centre of the horizontal density anomaly, the horizontal pressure difference is negative. This corresponds to the high-density region that has higher pressure than the surrounding, less dense water. The magnitude of the horizontal pressure difference increases with depth. From a radial distance of 750 m outwards, the horizontal pressure difference is positive. This is because horizontally the density is increasing as the distance approaches the shore where the isopycnals run parallel to the bottom slope.

The estimated azimuthal geostrophic velocities ($v_{\theta g}$) from (1.9) can be seen in Figure 3.4 b. The negative $v_{\theta g}$ are anti-cyclonic and correspond to the region of negative $\partial P \, \partial r^{-1}$ from panel a and the high-pressure core of the anomaly. Figure 3.4 b shows that from the centre of the anomaly to a radial distance of 750 m, $v_{\theta g}$ is anti-cyclonic. The anti-cyclonic values also increase with depth. The maximum anti-cyclonic $v_{\theta g}$ is estimated to be -0.02 m s^{-1} and occurs 250 m to the west and 330 m to the east of the centre of the horizontal density anomaly at a depth of 28.5 m. At this velocity, it would take a particle 25 or 33 hours to make one complete circuit at these radii. Using these values, $R_o \sim 0.5$ and 0.4. Beyond the radial distance of 750 m, $v_{\theta g}$ is cyclonic and increases with depth. The maximum cyclonic $v_{\theta g}$ is 0.029 m s^{-1} at a radial distance of 1030 m. This gives $R_o \sim 0.2$.

The estimated azimuthal cyclogeostrophic velocities ($v_{\theta cg}$) from (1.12) can be seen in Figure 3.4 c. Positive and negative azimuthal velocities indicate cyclonic and anti-cyclonic flow about the centre of the horizontal density anomaly. The distribution of $v_{\theta cg}$ is similar to that of $v_{\theta g}$ with one exception; there is a region near the centre that has no real or physical solution (the white region). Neglecting the white region for now, from the centre of the anomaly to a radial distance of approximately 750 m, $v_{\theta cg}$ is anti-cyclonic and increases in magnitude with depth. The maximum anti-cyclonic $v_{\theta cg}$ of -0.021 m s^{-1} occurs at a radius of 528 m which gives $R_o \sim$

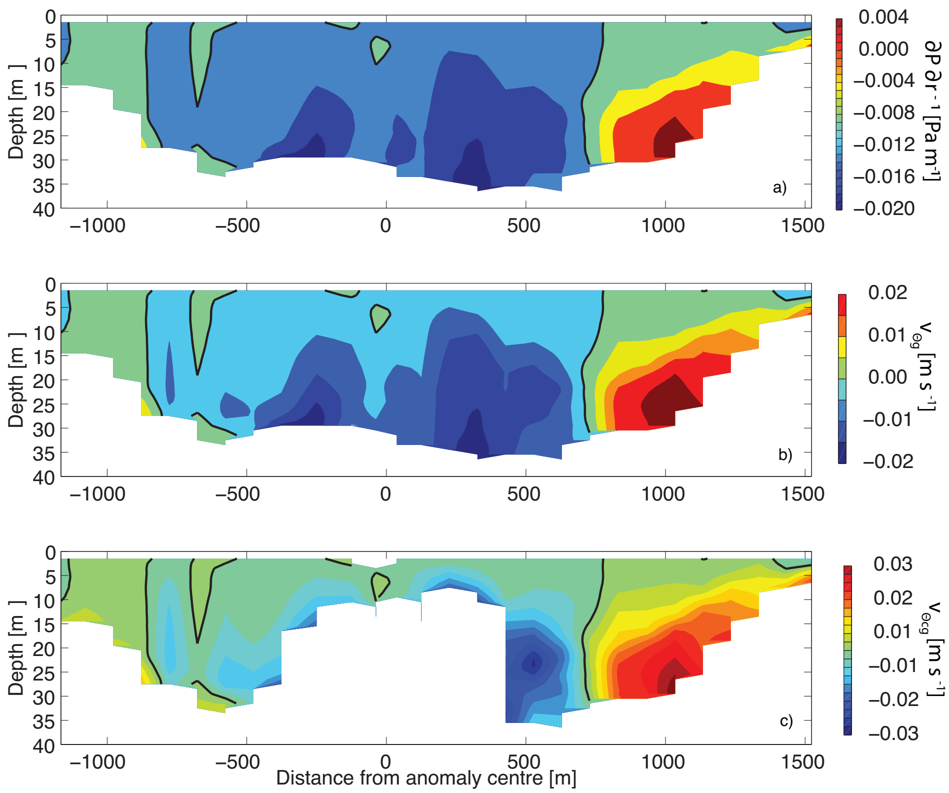

Figure 3.4: Contours of the horizontal pressure difference ($\partial P \partial r^{-1}$) [Pa m^{-1}] (panel a), $v_{\theta g}$ [m s^{-1}] (panel b), and $v_{\theta cg}$ (panel c) for the across-lake transect on 26 May 2013. The contour intervals for panel a) are 0.001 Pa m^{-1}, 0.005 m s^{-1} for panel b), and 0.0025 m s^{-1} for panel c). The distance along the x-axis is the radial distance from the centre of the density anomaly (0 m). Positive distances are to the east and negative distances are to the west. The solid black contour line represents in panels a), b) and c) represent $\partial P \, \partial r^{-1} = 0$, $v_{\theta g} = 0$, and $v_{\theta cg} = 0$. Positive and negative azimuthal velocities are cyclonic and anti-cyclonic.

0.3 and it would take a particle 45 hours to make one complete revolution at this speed and radius. Beyond 750 m, $v_{\theta cg}$ is cyclonic and increases in magnitude with depth. The maximum cyclonic $v_{\theta cg}$ of 0.021 m s^{-1} occurs at a radial distance of 1030 m and a depth of 29.5 m which gives $R_o \sim 0.15$. The region with no real and physical solution occurs, mathematically, when the radicand (the terms under the square root in 1.12) is less than zero. This occurs because the horizontal pressure force is more negative than the centripetal acceleration force is positive at that location (as discussed in section 1.3.4). While there may not be a solution in this region from the cyclogeostrophic balance, there are ways to estimate the azimuthal velocities in this region.

Before the azimuthal velocities can be estimated for white region in Figure 3.4 c, the estimates of $v_{\theta g}$ and $v_{\theta cg}$ are compared by non-dimensionalizing the difference between them ($v_{\theta cg} - v_{\theta g}$) by the mean of the velocities ($(v_{\theta cg} + v_{\theta g})/2$). This is shown in Figure 3.5 where the greatest difference (53 %) occurs at a radial distance of 130 m, and a depth of 14.5 m. This follows since the difference in the two balances is the inclusion of the centripetal acceleration force which has the greatest impact near the centre of the anomaly. The minimum difference (-16 %) occurs at a radial distance of 1030 m, and a depth of 29.5 m. The mean percent difference is 0.53 %. The mean value indicates that over the transect the difference in the two balances are negligible; however, there is a significant difference near the centre of the transect, which is of interest to this analysis.

To further investigate the importance of the centripetal acceleration force (F_c) in the cyclogeostrophic force balance, the values of F_c, Coriolis (F_{cor})

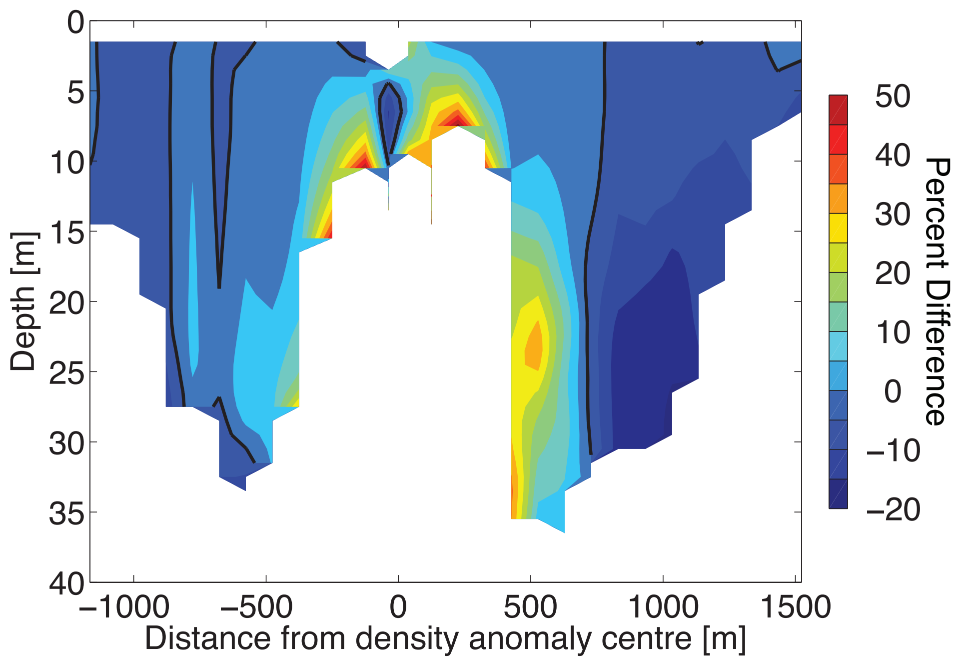

Figure 3.5: Contours of the percent difference in $v_{\theta cg}$ and $v_{\theta g}$ given by $(v_{\theta cg} - v_{\theta g})/((v_{\theta cg} + v_{\theta g})/2)100)$. Contour intervals of 5%.

and pressure difference (F_p) forces per unit mass were calculated and can be seen in panels a, b, and c) respectively in Figure 3.6. The maximum value of F_c is one order of magnitude smaller than F_{cor} and F_p. However, the greatest value occurs near the centre of the horizontal anomaly. The absolute value of each force per unit mass was also compared to the sum of the absolute values of all of the forces per unit mass and is presented as a percentage in Figure 3.7. Panel c shows that F_c has a range of 21 % (at a radial distance of 125 m) to 0.003 % (virtually no impact). This follows from $R_o \sim 0.2$. F_c was greatest near estimated R_{ri} of the horizontal density anomaly, and decreased radially outward. Panel b shows that F_{cor} has a range of 50 % to 42 %. Panel c shows that F_p has a range of 50% to 29

%. From this analysis, it can be seen that F_c has an impact on the force balance for radial distances less than 750 m; therefore, the horizontal density anomaly is in cyclogeostrophic balance.

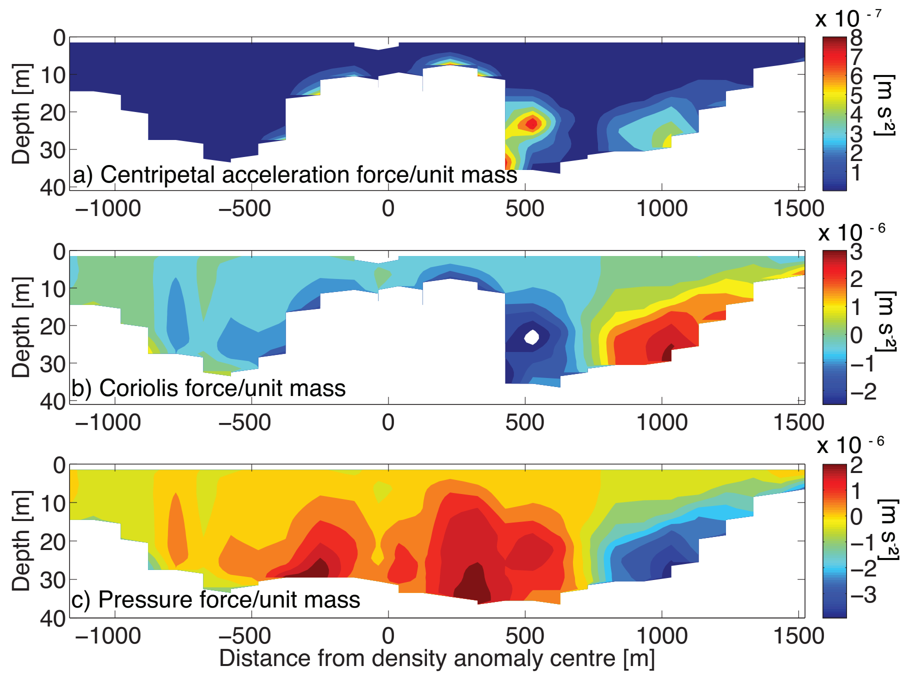

Figure 3.6: Contours of a) centripetal acceleration force per unit mass, b) Coriolis force per unit mass, and c) pressure force per unit mass for the across-lake transect collected on 26 May 2013. The contour intervals for panels a, b, and c are 1 x 10^{-7}, 0.5 x 10^{-6}, and 0.5 x 10^{-6} m s^{-2}. The distance along the x-axis is the radial distance from the centre of the density anomaly (0 m). Positive distances are to the east and negative distances are to the west.

An estimate of azimuthal velocity distribution for the entire transect is desired including the region where there is no real, physical solution for the cyclogeostrophic balance. As a first estimate, the values of $v_{\theta g}$ are applied to this region which can be seen in Figure 3.8 a. Similar to previous estimates, horizontally from 0 to an approximate radial distance of 750 m,

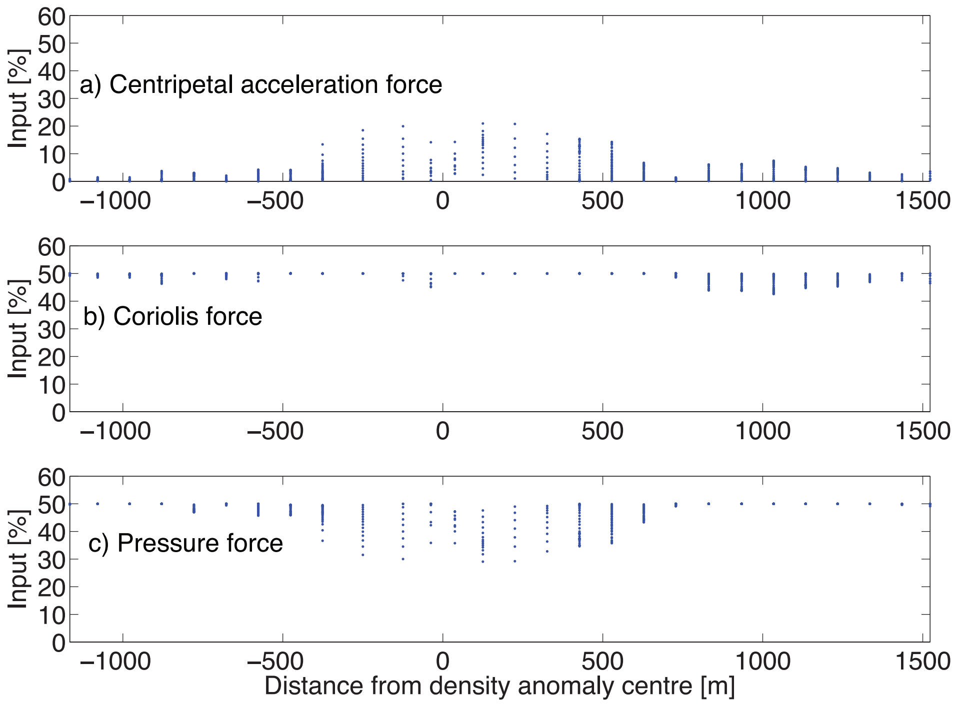

Figure 3.7: Percent of the absolute value of the a) centripetal acceleration force per unit mass, b) Coriolis force per unit mass, and c) pressure force per unit mass over the sum of the absolute value of the three forces for the across-lake transect collected on 26 May 2013. The distance along the x-axis is the radial distance from the centre of the density anomaly (0 m). Positive distances are to the east and negative distances are to the west.

the azimuthal velocity is anti-cyclonic and reaches a maximum anti-cyclonic velocity at 520 m. After this distance, the velocity magnitude decreases, until 750 m, where it transitions from anti-cyclonic to cyclonic. Vertically in the anti-cyclonic region, the magnitude of the azimuthal velocity increases with depth until 23.5 m, and then decreases to the bottom.

Another estimate for the distribution of $v_{\theta cg}$ is using one of the components of the cyclogeostrophic solution. When regions have no real and physical solution, a solution still exists; however, it is a complex solution

($v_{comp} = v_{real} + iv_{imag}$) where v_{real} is the real component in the azimuthal direction and v_{imag} is the imaginary component in the radial direction. The complete distribution of $v_{\theta cg}$ can be estimated using v_{real} which is the same as solving the cyclogeostrophic equation using the minimum allowable pressure difference. This is shown in Figure 3.8 b. This estimate results in a similar pattern as the previous estimate with the maximum anti-cyclonic azimuthal velocity occurring at 380 m and a depth of 29.5 m. For this estimate, the azimuthal velocity inside the horizontal density anomaly increases with depth until it reaches the maximum magnitude, and then is uniform to the bottom.

The difference between the two estimates is shown in Figure 3.8 c which shows the difference in the first and second estimate non-dimensionalized by the mean of the two estimates. The greatest percent difference occurs near the centre of the horizontal density anomaly at 40 m near the bottom.

The existence of complex solutions near the centre of the horizontal density anomaly indicates that there is a radial component to the velocity and that the initial assumption that the density anomaly has no radial velocity is not entirely accurate. The radial velocity component is equivalent to v_{imag} of the complex solution and is shown in Figure 3.8 d. This shows that v_{imag} only exists where there is no real and physical solution to $v_{\theta cg}$, and that it increases away from the centre of the anomaly to a radial distance of 250 m, and increases vertically with depth. v_{imag} ranges from 0 to 0.0175 m s^{-1}, and has a mean of 0.001 m s^{-1}. This indicates that the horizontal density anomaly was not steady; however, since these transects are a snapshot in time and the full transects were not repeated, the data collected cannot be used to determine whether or not the horizontal density anomaly is steady, spinning-up or spinning-down. To investigate motion at one time, the steady assumption is an appropriate first estimate.

The same methods of estimating $v_{\theta g}$ and $v_{\theta cg}$ were used for the along-lake transect with similar results shown in Figure 3.9 where panels a through f correspond to depths of 5, 10, 15, 20, 25, and 30 m. The azimuthal velocity estimates start at a radial distance of 200 m because the along-lake transect did not cross through the centre of the horizontal density anomaly. From Figure 3.9, the velocity magnitudes decrease with radial distance and transition from anti-cyclonic to cyclonic. The velocities also increase in magnitude with depth. The greatest difference between $v_{\theta g}$ and $v_{\theta cg}$ occurs within 250 m of the centre of the horizontal density anomaly. This is similar to the results from the across-lake transect and this is expected due to the inclusion of the centripetal acceleration force in the cyclogeostrophic balance.

To determine whether the estimates of $v_{\theta cg}$ are reasonable, they are compared to the measured ADCP velocities. Since the ADCP was located at a radial distance of 1330 m, which is outside the region where there is no real and physical solution, the patched estimates can not be compared to these measured velocities. The azimuthal component of the ADCP velocities ($v_{\theta A}$) are compared to $v_{\theta g}$ and $v_{\theta cg}$ at similar radial distances and are shown in Figure 3.10 a. $v_{\theta A}$ is anti-cyclonic and decreases in magnitude with depth. $v_{\theta g}$ and $v_{\theta cg}$ are cyclonic and increase in magnitude with depth. $v_{\theta A}$, $v_{\theta g}$, and $v_{\theta cg}$ have a similar slope in panel a. However, $v_{\theta A}$ approaches 0 m s^{-1} near the bottom, and $v_{\theta g}$, and $v_{\theta cg}$ approach 0 m s^{-1} near the surface. $v_{\theta g}$

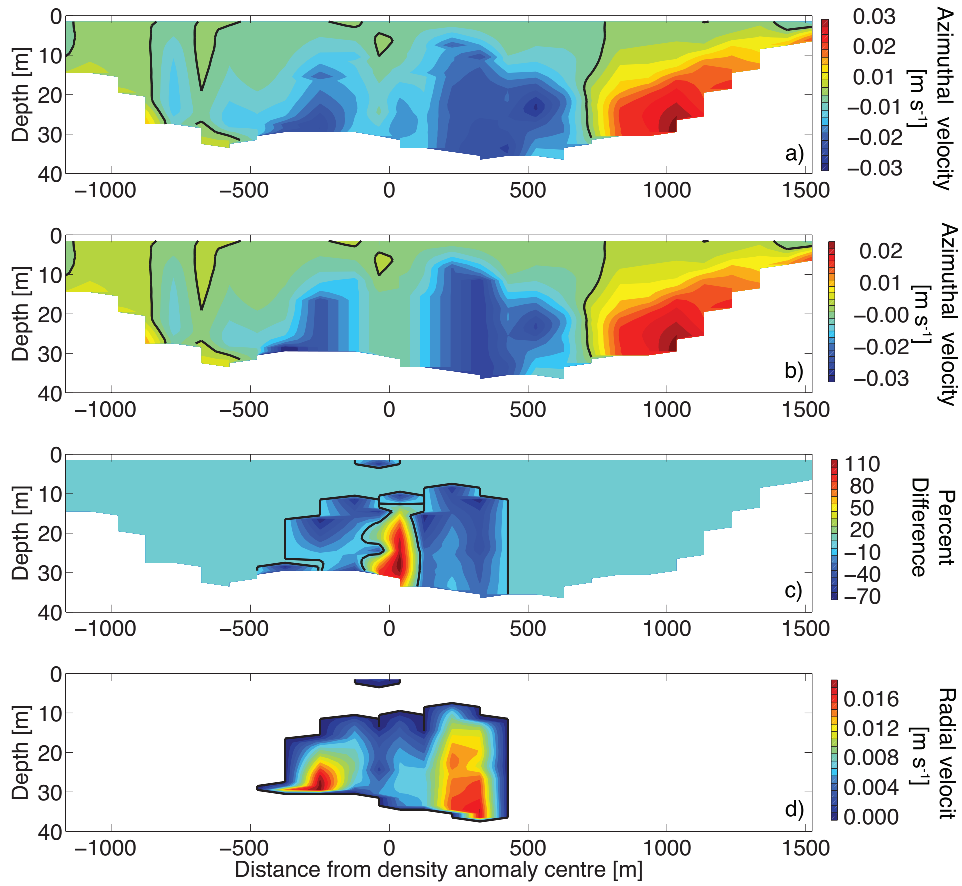

Figure 3.8: Contours of a) $v_{\theta cg}$ patched with $v_{\theta g}$, b) $v_{\theta cg}$ patched with v_{real} from the cyclogeostrophic balance solution, c) the percent difference of panels a and b non-dimensionalized by the mean of the two solutions, and d) v_{imag} component of the cyclogeostrophic velocity. Panel a and b have contour intervals of 0.0025 m s^{-1}, panel c has intervals of 10 %, and panel d has intervals of 0.001 m s^{-1}. Positive and negative values of azimuthal velocity are cyclonic and anti-cyclonic. The distance along the x-axis is the radial distance from the centre of the density anomaly (0 m) with positive distances to the east and negative distances to the west. The solid black contour line represents values of 0 m s^{-1} for a, b and d, and 0 % for c.

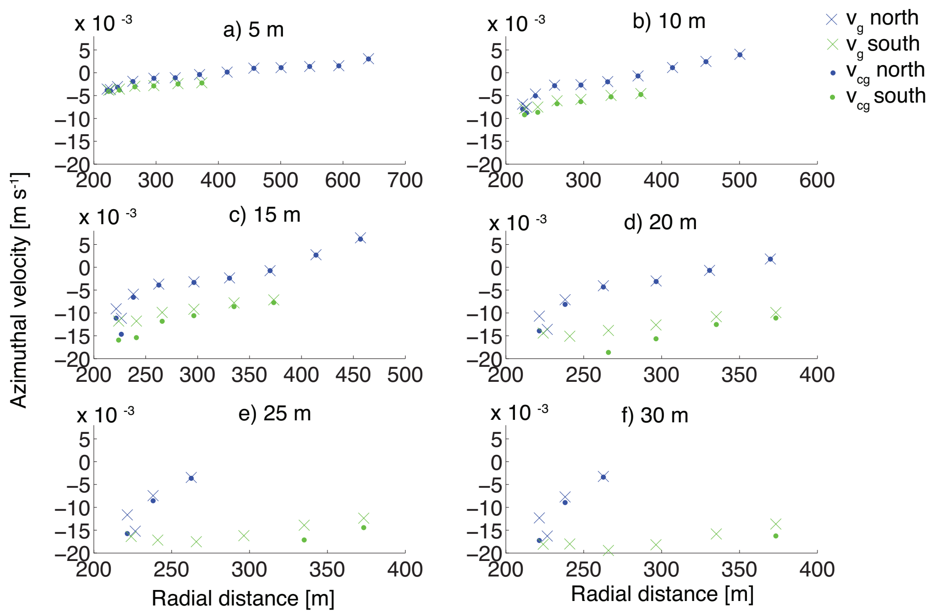

Figure 3.9: Panels a, b, c, d, e, and f show estimates of $v_{\theta g}$ and $v_{\theta cg}$ for depths of 5, 10, 15, 20, 25, and 30 m. Xs marks $v_{\theta g}$ and the dots marks $v_{\theta cg}$. Blue markers are to north of intersection of the across and along-lake transects and green markers are to the south. Positive and negative azimuthal velocities are cyclonic and anti-cyclonic.

and $v_{\theta cg}$ approach 0 m s^{-1} near the surface because the surface was initially assumed to be the level of no-motion. $v_{\theta A}$ (which comes from a direct measurement of velocity) shows that the azimuthal velocity near the surface is not zero, and that the level of no-motion is approximately the bottom. When the magnitude of $v_{\theta A}$ near the surface (0.027 m s^{-1}) is subtracted from the estimated $v_{\theta g}$ and $v_{\theta cg}$ (at similar radial distance) the adjusted $v_{\theta g}$ and $v_{\theta cg}$ have similar values and follow the same pattern as the measured $v_{\theta A}$ shown in Figure 3.10 b. This indicates that the assumption that the surface is the level of no-motion is incorrect, and that the level of no-motion is near the bottom.

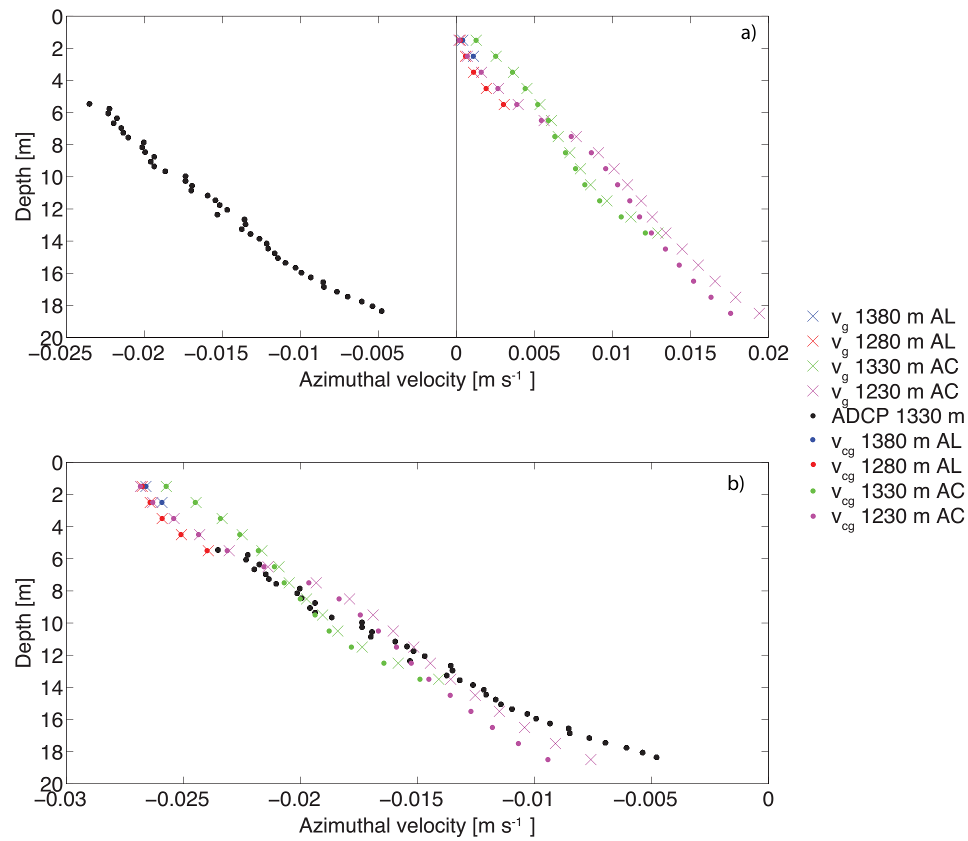

Figure 3.10: Panel a) comparison of $v_{\theta A}$ to $v_{\theta cg}$ and $v_{\theta g}$ [m s^{-1}] at comparable radial distances on the across (AC) and along-lake (AL) transects and panel b) corrected comparison for level of no-motion at the bottom.

The previously estimated patched distributions of $v_{\theta cg}$ were based on the assumption that the level of no-motion was at the surface and which was achieved by integrating down from the surface. Since the measured ADCP azimuthal velocities indicate that the level of no-motion is at the bottom, these estimate may not be representative of the actual distribution. To estimate $v_{\theta cg}$ with the level of no-motion at the bottom, the transect should be integrated up from the bottom; however, since the lake bottom is not flat this is difficult to do; therefore, $v_{\theta cg}$ at the bottom of each profile was subtracted over the entire depth of the profile for the entire distribution. This was done to both the estimated distributions of $v_{\theta cg}$ patched with $v_{\theta g}$ and with the real component of $v_{\theta g}$ which can be seen in panels a and b of Figure 3.11. The distributions are nearly vertical inversions of the original estimated distributions; however, the circulations are in the opposite direction. From beneath the ice surface downwards, the circulations are cyclonic for 0 to 750 m. There are small regions near the bottom at 100 m and 500 m in panel a, and 500 m in panel b where the flow is anti-cyclonic. From 750 m radially outwards, the flow is anti-cyclonic. Unlike the initial estimated distributions, the magnitudes of the azimuthal velocities decrease with depth. Also, near the centre of the horizontal density anomaly, there is a depth beneath which the circulation transitions from cyclonic to anti-cyclonic.

3.2 2014 Results

At the beginning of the 2014 field campaign, the ice had a mean thickness of 1.0 m with a layer of snow and slush that was 0.05 to 0.20 m thick on top. The ice thickness decreased by 0.15 to 0.35 m over the period of study; however in contrast to 2013, no moats formed. The mean daily air temperature over the period of study was 3.5°C. The mean wind speed was 13 km hr^{-1} from 19 to 26 May 2014 with a mean direction of 209°.

Ten CTD transects were collected during the period of study and all show that the temperatures measured were below 4°C. The across and along-

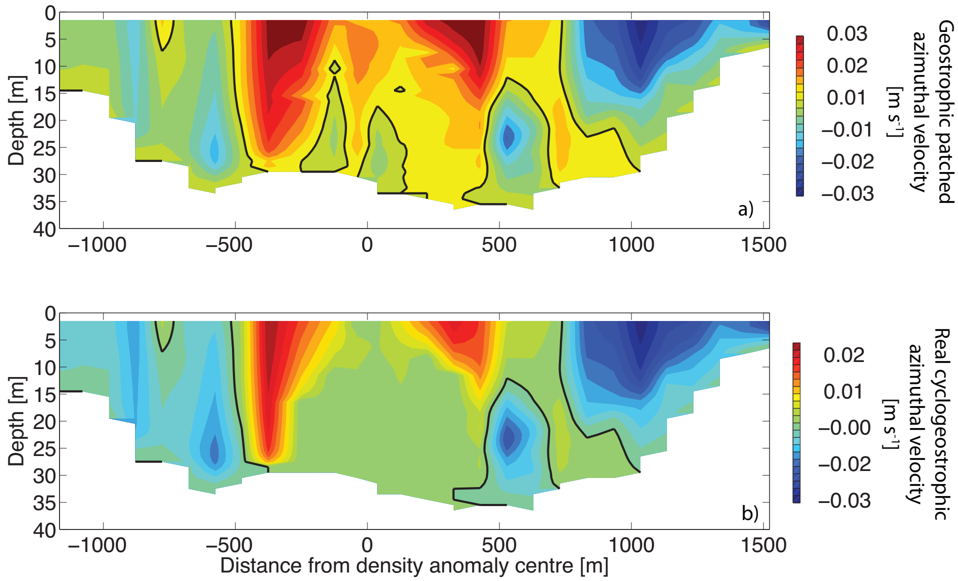

Figure 3.11: Contours of distribution of $v_{\theta cg}$ patched with $v_{\theta g}$ (panel a) and v_{real} (panel b) corrected for level of no-motion at the bottom for across-lake transect collected on 26 May 2013. Contour intervals of 0.0025 m s^{-1}. Positive and negative azimuthal velocities are cyclonic and anti-cyclonic.

lake temperature distributions collected on 26 May 2014 (panels a and b of Figure 3.12) are representative of the 10 transects. From the distributions of water temperature, it can be seen that the water temperature increases with depth (inversely stratified) and is vertically stable. If the lake was horizontally stable, the isotherms would be horizontal; however, Figure 3.12 a shows horizontal variation in temperature, though much less than observed in 2013. From the east to west, the temperature decreases horizontally until approximately 1500 m from the east shore. Here, it begins to increase with distance. This causes a slight upward curve (concavity) in the isotherms over the width of the lake.

Similar to the 2013 results, conductivities were low; therefore, the tem-

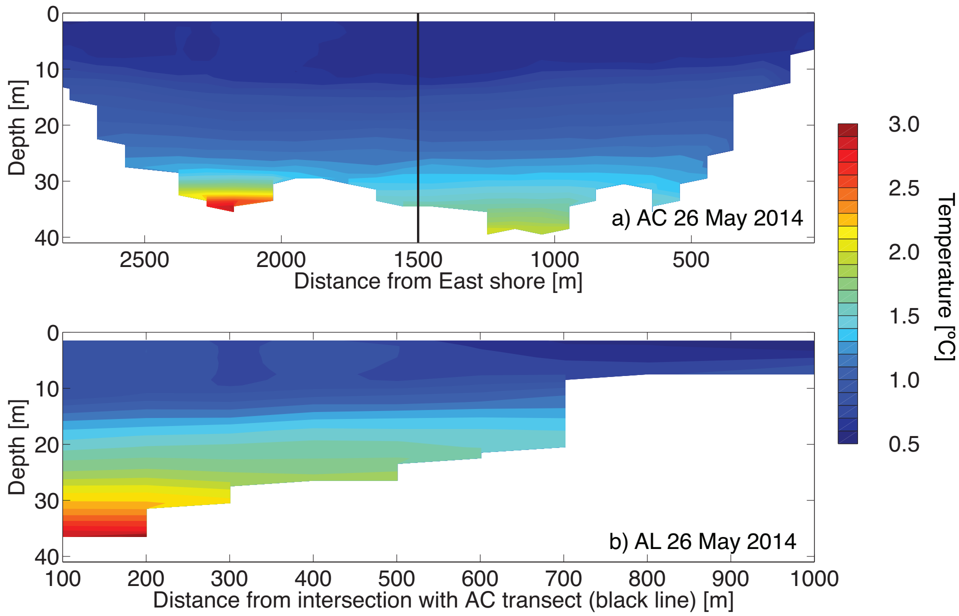

Figure 3.12: Contours of temperature for the across (AC) and along-lake (AL) transects (panels a and b) 26 May 2014 with contour intervals of 0.05 °C. The data has been vertically averaged every 1 m. The distance along the x-axis is the distance from the eastern shore (panel a) and distance from the intersection of the two transects (panel b). The black vertical line in panel a is where the two transects intersected along the across-lake transect at $\sim 90°$.

perature and density distributions follow similar patterns. Since there is horizontal variation in temperature, there is also horizontal variation in density. Horizontally, there is less dense water at the centre of the lake with denser water on either side. This creates an upward concavity in the isopycnals. The denser water near the shores applies an inward directed pressure force on the less dense water in the centre. This creates a low-pressure horizontal density anomaly in the centre of the lake. This isopycnal concavity was present for the 7-day observation period; therefore, the anomaly is assumed to be steady. Since the denser water did not flow inward under the less dense water (which would have flowed outward and over), there must have been a force opposing the inward pressure force from the denser fluid. This indicates that there was a balance of forces and since the concavity of the anomaly was over the entire width of the lake, it is possible that the balance could be geostrophic, cyclogeostrophic, or cyclostrophic.

The maximum horizontal variation in density, in the top 20 m of the water column, is used to estimate the type of balance and was found to be 0.0088 kg m^{-3} at a depth of 12.5 m. This gives *g'* of 8.63 x 10^{-5} m s^{-2}. Assuming a height of 12.5 m (the height over which the isopycnals appear to be concave), $R_{ri} \sim 240$ m. This radius is less than the horizontal length of the concavity of the isopycnals $\sim$ 2000 m which indicates that the circulation is modified by the earth's rotation and is in either geostrophic or cyclogeostrophic balance. Using R_{ri} and L $\sim$ 2000 m, R_o is 0.12 which does not immediately indicate which balance the circulation is subject to.

Since R_{ri} and R_o do not immediately indicate the type of balance, both geostrophic and cyclogeostrophic balances are investigated to determine the difference between the two. Both balances depend on the presence of a horizontal pressure difference; therefore, $\partial P \, \partial r^{-1}$ was calculated moving away from the centre of the anomaly, and assuming that the level of no-motion is directly beneath the ice surface. This can be seen in Figure 3.13 a. In the top 10 m of the water column, $\partial P \, \partial r^{-1}$ increases laterally to the west until 250 m, then decreases until it reaches a minimum at approximately 1000 m. $\partial P \, \partial r^{-1}$ also increases in magnitude with depth in the top 10 m. Below 10 m, $\partial P \, \partial r^{-1}$ increases radially outward from the centre until approximately 500 m to the east and all the way to the sloping boundary to the west. This shows that the centre of the anomaly is a low-pressure centre. $\partial P\,\partial r^{-1}$ also increases with depth from 10 m until the bottom.

Using the same methods as mentioned in the previous section (Section 3.1), $v_{\theta g}$ and $v_{\theta cg}$ are estimated for the transect and can be seen in panels b and c in Figure 3.13. $\partial P\,\partial r^{-1}$, $v_{\theta g}$, and $v_{\theta cg}$ have similar patterns where positive $\partial P\,\partial r^{-1}$ values correspond to cyclonic motion and negative values correspond to anti-cyclonic motion. Since this is a low-pressure horizontal density anomaly, there is a solution everywhere for the cyclogeostrophic estimated because $\partial P\,\partial r^{-1}$ is positive in the core and the radicand is always real. The estimates of azimuthal velocity distribution show that there is a shallow (0 - 10 m) anti-cyclonic horizontal anomaly above a cyclonically rotating anomaly that reaches from 10 m to the bottom boundary. The two circulations are not directly on top of one another, the upper anti-cyclonic anomaly is shifted to the east by approximately 100 m. Both maximum $v_{\theta g}$ and $v_{\theta cg}$, 0.0063 and 0.0059 m s^{-1}, occur 764 m to the west of the centre of the anomaly. Using (1.4), this gives $R_o \sim 0.06$. Minimum $v_{\theta g}$ and $v_{\theta cg}$, -0.0030 and -0.0033 m s^{-1}, occur 278 m to the east of the centre of the anomaly which gives $R_o \sim 0.08$. The difference between $v_{\theta cg}$ and $v_{\theta g}$ is non-dimensionalized by the mean of the two values and is presented as a percentage in Figure 3.13 d. The greatest positive percent difference of 9 % occurs at 280 m and a depth of 8.5 m and is due to $v_{\theta cg}$ being greater than $v_{\theta g}$s. The greatest negative percent difference is due to $v_{\theta g}$ being greater than $v_{\theta cg}$, -19 %, occurs at 75 m and 33.5 depth. Both these locations are inside the estimated R_{ri} and are near the centre.

To further investigate the importance of F_c in the cyclogeostrophic force

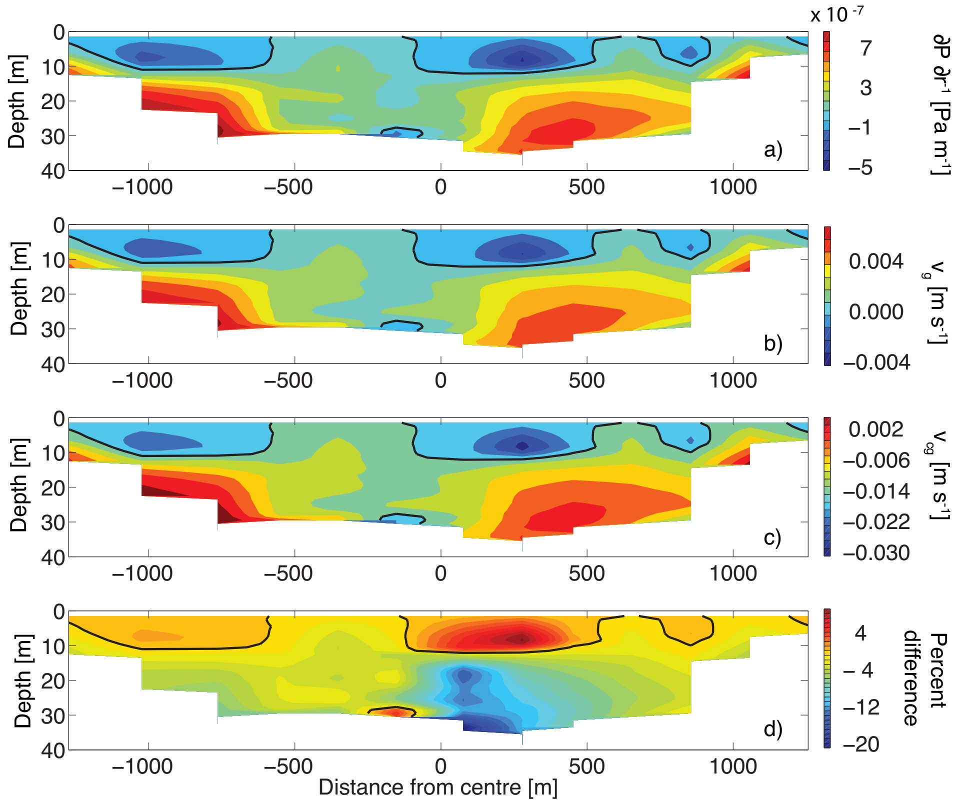

Figure 3.13: $\partial P\,\partial r^{-1}$ for 26 May 2014 in panel a, $v_{\theta g}$ in panel b, $v_{\theta cg}$ in panel c, and the difference between $v_{\theta cg}$ and $v_{\theta g}$ non-dimensionalized by the mean of the two values (as a percentage). The contour interval for a is 1 x 10^{-7} Pa m^{-1} for panel a, 0.001 m s^{-1} for panels b and c, and 1 % for panel d. Positive and negative values of azimuthal velocity are cyclonic and anti-cyclonic. The distance along the x-axis is the radial distance from the centre of the density anomaly (0 m) with positive distances to the east and negative distances to the west. The solid black contour line represents values of 0 Pa m^{-1} for a, 0 m s^{-1} for b and c, and 0 % for d.

balance, the values of F_c, F_{cor}, and F_p per unit mass were calculated and can be seen in Figure 3.14. Below 10 m in panel a, F_c increases with radial distance and depth until it reaches its maximum value at the bottom at a radial distance of 250 m. It then decreases with increasing radial distance from 0 m to 10 m, there is also an input from F_c at 5 m depth and 250 m radius. For F_{cor} below 10 m in panel b, the input increases with radial distance and depth, until it reaches the maximum value at the bottom of the 250 m radial distance. The values then decrease with increasing radius. From 0 to 10 m, F_c decreases with radial distance to 250 m, and depth to 5 m. Then, the values increases with depth to 10 m and with radial distance. The distribution of F_{press} follows that of F_{cor} except that where F_{cor} was positive, F_{pre} is negative and vice versa. When comparing the magnitudes, it can be seen that the maximum value of F_c is one order of magnitude smaller than F_{cor} and F_{press}.

As another method of comparison, the percent input from each of the three terms was calculated (the absolute value of each term divided by the sum of all the absolute values of the terms). The percent input forF_{cor} and F_{press} range from 40 to 50 % over the entire transect whereas F_c ranges from 0 to 9 %, with a mean value of 2 %. The greatest value of F_c occurs at the centre of the horizontal anomaly and decreases radially outward; therefore, F_c impacts the force balance within a radial distance 500 m.

No ADCP measurements were available to compare to the estimates of $v_{\theta g}$ and $v_{\theta cg}$, so the estimates were left as is with no correction for different levels of no-motion.

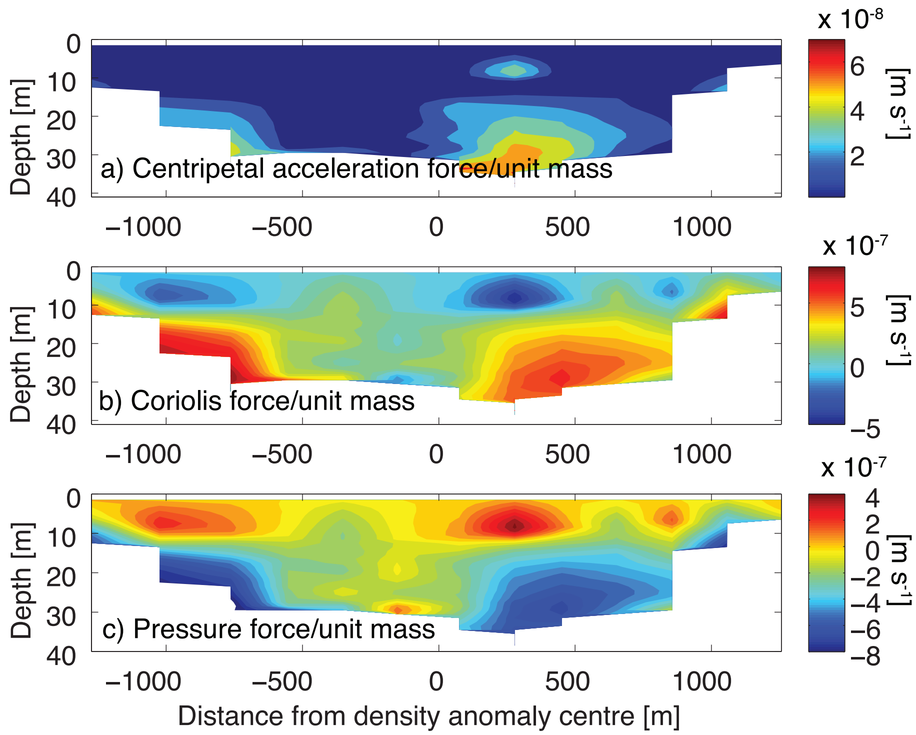

Figure 3.14: Contours of a) centripetal acceleration force per unit mass, b) Coriolis force per unit mass, and c) pressure force per unit mass for the across-lake transect collected on 26 May 2014. The contour interval for panel a is 1 x 10^{-8} m s^{-2}, and 1 x 10^{-7} m s^{-2} for panels b and c. The distance along the x-axis is the radial distance from the centre of the density anomaly (0 m). Positive distances are to the east and negative distances are to the west.

Chapter 4

Discussion

This chapter will first separately discuss the results of the field campaigns, presented in chapter 3, and then will compare the results between years.

4.1 2013 Data Discussion

In 2013, the thermal and density structures were vertically stable; however, there was distinct horizontal temperature and density variation near the centre of the lake where there was a cylindrical core of denser, warmer water. This denser water exerted an outward pressure force on the less dense water surrounding it. When in steady state and modified by the earth's rotation, an anti-cyclonic, rotating horizontal density anomaly extended from the surface down paired with a weaker, less defined cyclonic circulation that extends from near the bottom upwards.

The observed anomaly had a radius ~ 350 m, which is twice $R_{ri} \sim 160$ m which indicated that the anomaly was affected by the earth's rotation. R_{ri} of 160 m is comparable to the estimate of $R_{ri} \sim 200$ m for the anomaly observed in Pavilion Lake (*Forrest et al.*, 2013), and $R_{ri} \sim 220$ m estimated for the anomaly observed in Lake Pääjärvi (*Rizk et al.*, 2014). All of these estimates are much smaller than the estimated $R_{ri} \sim 10$ km for anomalies under sea-ice (*Timmermans et al.*, 2008).

R_o for the 2013 observations was estimated, using the observed density differences, to be ~ 0.2. This is less than the estimated R_o of 1.7 for the Pavilion Lake cyclogeostrophic anomaly (*Forrest et al.*, 2013) and those estimated for the cyclogeostrophic anomalies under sea-ice ($R_o \sim 0.5$ to 0.99) (*Timmermans et al.*, 2008). An R_o of 0.2 does not immediately indicate whether the anomaly is in geostrophic or cyclogeostrophic balance; therefore, both balances were investigated by estimating their associated azimuthal velocities and comparing them.

The distributions of $v_{\theta g}$ and $v_{\theta cg}$ were estimated; however, the horizontal density differences near the centre of the anomaly were unable to support a purely azimuthal cyclogeostrophic balance. This resulted in radial velocities and $v_{\theta cg}$ had a complex solution near the centre of the anomaly. No other observation of horizontal anomalies in lakes have had this issue. This could be because previous observations did not have high enough resolution near the centre of the anomaly. Two possible methods were investigated to complete the cyclogeostrophic solution: 1) using the geostrophic azimuthal velocities, and 2) using the real component of the complex solution. Since very little is known about the region at the centre of high-pressure cyclogeostrophic anomalies, and the two methods did not vary significantly, either method is acceptable as a first estimate. When the complete distribution of $v_{\theta cg}$ was compared to $v_{\theta g}$, they were found to be comparable, and only vary slightly near the centre (due to the difference in centripetal acceleration force inclusion) and near the estimated R_{ri}.

To calculate the azimuthal velocities, the level of no-motion was taken at the surface as a first estimation, this resulted in an anti-cyclonic anomaly in the bottom region of the lake. However, comparing the azimuthal velocities to the measured azimuthal ADCP velocities, suggests the level of no-motion is actually near the bottom. To address this issue, the balances should have been solved by integrating the force balance up from the bottom as opposed to down from the top when the level of no-motion is at the surface. However, since the lake's bottom is not flat, it is difficult to do this without a three dimensional model. Therefore, the estimated azimuthal velocity at the bottom of each profile was subtracted from the entire profile so that the level of no-motion is at the bottom. This is a reasonable first estimate for the level of no-motion being at the bottom. This caused the horizontal density anomaly to be contained in the upper portion of the lake and the direction of the circulation to switch direction. This is similar to the density anomaly observed by *Forrest et al.* (2013) which was assumed to be contained in the top layer; however, that level of no-motion was assumed at the surface which reduced the interaction with the lake bottom.

Prior to adjusting the estimates of azimuthal velocity for the level of no-motion at the bottom, the distributions did not show paired cyclonic and anti-cyclonic rotations; however, once adjusted, the cyclonic anomaly in the surface layer is paired with a weak anti-cyclonic anomaly in the bottom layer. This is similar to the anomalies observed in lakes by *Forrest et al.* (2013), and *Rizk et al.* (2014), in oceans by *Timmermans et al.* (2008), and predicted in lake models by *Huttula et al.* (2010).

The 2013 estimate of maximum anti-cyclonic $v_{\theta g}$ and $v_{\theta cg}$ are on the order of 0.02 m s^{-1}, and the maximum cyclonic velocities are on the order of 0.03 m s^{-1}. These are comparable to observations made in Pavilion Lake where the the maximum cyclonic velocity was 0.021 m s^{-1} (*Forrest et al.*, 2013). These estimated velocities are greater than the maximum 0.001 m s^{-1} estimated in Lake Pääjärvi (*Rizk et al.*, 2014), and the observed horizontal velocities in Tub Lake of 3.047 x 10^{-4} m s^{-1} near the shore and 4.05 x 10^{-4} m s^{-1} at the centre (*Likens and Ragotzkie*, 1966).

It is hypothesized that the rotating circulation observed was driven by heat flux at the shorelines from incoming warm streams (*Kirillin et al.*, 2015) and the heating of the water in the moats. The water entering the moats came from snow melt and was much warmer than the lake water because it was subject to solar heating as it travelled over land and through the streams. This warmer, denser water created a dense underflow that ran down the slopes of the shore and converged towards the lake center, where it produced an upwelling of warmer denser water. From continuity, this upwelling needed to be balanced by a radial outward flow which was in the form of return flow across the bulk water column. This flow was then deflected to the right by the Coriolis force. This is similar to the pattern of mid-winter circulation proposed by *Welch and Bergmann* which was driven by heat release from the sediment and freeze out (1985). This density driven flow was also observed by *Rhines* (1998) in experiments. However, the 2013 circulation has a different hypothesized driving mechanism of the warm incoming streams which has also been proposed by *Salonen et al.* (2014) and compared to circulation forced by differential surface heating.

There are two distinct regions in the 2013 observations: 1) the rotating horizontal density anomaly in the centre of the lake, and 2) flow down the slopes of the lake. As discussed previously, rotating horizontal density anomalies have been inferred from previous observations and model predictions (*Likens and Ragotzkie*, 1966; *Huttula et al.*, 2010; *Forrest et al.*, 2013; *Rizk et al.*, 2014); however, their formation and forcing mechanisms have not been determined. Flow down slopes driven by heat release from the sediment has been suggested by *Mortimer and Mackereth* (1958) and similar flows have been observed by *Likens and Ragotzkie* (1966), *Welch and Bergmann* (1985) and *Malm* (1998); however, it has not been observed, outside the laboratory, to be forced by warm, dense inflow from streams during the end of winter.

4.2 2014 Data Discussion

The nearly horizontal isotherms and isopycnals observed near the centre of the lake in 2014 are expected in ice-covered lakes in winter when the lake is vertically stable and inversely stratified (*Wetzel*, 1975; *Welch and Bergmann*, 1985). It is also expected that the lake be horizontally stable with little horizontal temperature variability; however, when the entire lake transect is inspected, there are horizontal density differences that cause slight upward concavity in the isotherms and isopycnals over the width of the lake. This causes an inward directed pressure force which, when modified by the earth's rotation, caused vertically paired, rotating horizontal density anomalies. These horizontal density anomalies can be compared to similar observations and predictions with R_{ri}, R_o, and azimuthal velocity.

R_{ri} for the observed cyclonic rotating anomaly was estimated, using the observed horizontal density differences, to be 240 m which is less than the observed length of the tilted isopycnals ($\sim$ 1000 m). This R_{ri} is comparable to the estimate for $R_{ri} \sim 200$ m from the anomaly observed by *Forrest et al.* in Pavilion Lake, British Columbia where the observed radius of the anomaly was 110 m (2013). *Rizk et al.* estimated that $R_{ri} \sim 220$ m which was one order of magnitude smaller than the observed length scale of the anomaly observed in Lake Pääjärvi. Since the observed radii were greater than or on the order of R_{ri}, the observed anomalies were modified by the earth's rotation which is further investigated by calculating R_o. R_o was initially estimated to be 0.12 for the observed system. This is less than $R_o \sim 1.7$ estimated for Pavilion Lake where the system was assumed to be in cyclogeostrophic balance (*Forrest et al.*, 2013). The 2014 R_o is on the order of the upper limit of the range of $R_o \sim 10^{-3}$ to 10^{-2} estimated for Lake Pääjärvi where the anomalies were assumed to be in geostrophic balance (*Rizk et al.*, 2014). R_o values of 0.5 to 0.99 have been estimated for the rotating anomalies in cyclogeostrophic balance observed under sea-ice (*Timmermans et al.*, 2008).

R_o of 0.12 does not strongly indicate whether the observed system was in geostrophic or cyclogeostrophic balance; therefore, both balances were estimated and compared. The estimations of $v_{\theta g}$ and $v_{\theta cg}$ show the same pattern and the values do not vary significantly. They did vary near in the centre which is expected because this is where the centripetal acceleration force has the greatest impact and its inclusion is the difference between the two balances. Therefore, assuming one balance as opposed to the other would not result in significantly different azimuthal velocity distributions.

For the anomalies in 2014, the maximum magnitudes of the cyclonic and anti-cyclonic azimuthal velocities (for both geostrophic and cyclogeostrophic balances) were 0.006 and 0.003 m s^{-1}. These velocities are on the same order of magnitude as those estimated in Lake Pääjärvi which were on the order of 0.001 m s^{-1} (*Rizk et al.*, 2014). The velocities are greater than observations made in Tub Lake of 3.047 x 10^{-4} m s^{-1} near the shores and 4.05 x 10^{-4} m s^{-1} near the centre (*Likens and Ragotzkie*, 1966). However, the estimates are less than those from Pavilion Lake (0.021 m s^{-1}) (*Forrest et al.*, 2013) and 0.01 m s^{-1} (*Huttula et al.*, 2010) under lake-ice as well as under sea-ice (0.09 to 0.26 m s^{-1}) (*Timmermans et al.*, 2008).

From 0 to 10 m depth, there was a weak, anti-cyclonically rotating density anomaly, and from 10 to the bottom, there was a slightly stronger, cyclonically rotating, horizontal density anomaly. The transition from anti-cyclonic to cyclonic represents a level of no-motion at 10 m. Vertically paired rotating density anomalies have been observed under ice in lakes by *Forrest et al.* (2013), and *Rizk et al.* (2014), as well as in the ocean under sea-ice by *Timmermans et al.* (2008). *Huttula et al.* (2010) also predicted vertically paired anti-cyclonic and cyclonic rotating density anomalies in the top and bottom of Lake Pääjärvi using the Princeton Ocean Model. These observations typically refer to one rotating anomaly even though it is paired. The anomaly that is referred to is considered the dominant anomaly, usually, because it has the greater thickness and sometimes a greater velocity.

It is hypothesized that the horizontal density anomaly, which was evident from the upward concavity in the isotherms and isopycnals, was formed when the ice-cover initially formed and heat was released from the sediment into the overlying water causing an increase in water density just above the boundaries. This release of heat would have been greater closer to the shores which would account for the upward tilt in the isotherms. There was no other source of heat in 2014 because at the time of observation the entire lake was covered in ice and snow which insulated and protected the water column from solar radiation (*Arst et al.*, 2006). Since there was no significant source or sink of heat, the slight horizontal density anomaly was able to persist and was balanced by the Coriolis force causing cyclonic flow about the low-pressure (lower-density) centre. This is similar to the observations and model predictions for Lake Pääjärvi made by *Rizk et al.* (2014) where it was assumed that if the thermal regime of the lake was only controlled by the input of heat from the sediment, water temperatures near the shores would increase and cause cyclonic rotation. Heat release from the sediment is also assumed to be the cause of convection that drove circulation in Tub Lake (*Likens and Ragotzkie*, 1966).

4.3 2013 and 2014 Comparison

Observations from both field seasons measured water temperatures below 4°C, had vertically stable density profiles, and horizontal density variation. However, the horizontal density patterns observed in the two years were different and caused basin-wide water circulations in opposing directions. In 2013, there was a dominant, high-pressure horizontal density anomaly near the centre of the lake. If the level of no-motion is assumed to be directly beneath the ice-surface, the anomaly is in the bottom of the lake and is anti-cyclonic. If the level of no-motion is assumed to be at the bottom, which is supported by ACDP measurements, there is a strong cyclonic rotation in the upper region of the lake and an anti-cyclonic rotating anomaly in the bottom layer of the lake. In 2014, there was a dominant low-pressure cyclonic density anomaly near the centre of the lake in the bottom region, and a weak anti-cyclonic anomaly in the upper region. The observations between the two years have similarities as well as differences.

The observed radii of the anomalies (1000 m for 2014 and 350 m for 2013) and the estimated R_{ri} ($\sim$ 240 m for 2014 and 160 m for 2013) are comparable. The estimates of R_o for the two years are also comparable with $R_o \sim 0.12$ for 2014 and 0.2 for 2013. In both years, it was not evident which force balance, geostrophic or cyclogeostrophic, was relevant. When the azimuthal velocities (v_θ) for both balances were estimated, it was found that they did not vary significantly; therefore, the choice of either balance would not greatly affect the results. However, the magnitudes of v_θ were an order of magnitude different between years. In 2014, the maximum cyclonic and anti-cyclonic v_θ were 0.006 and 0.003 m s^{-1}, whereas in 2013, the maximum cyclonic and anti-cyclonic v_θ 0.03 and 0.02 m s^{-1}. Both years had paired rotating anomalies.

The differences in the observations is hypothesized to come from the difference in the length of time from when the observations were made to when ice-off occurred. In 2013, the observations were made at, during and after ice-off. In 2014, ice-off did not occur until 18 June, 12 days after the last day of study. This time difference allowed for variations in the ice and snow-cover. In 2013, there were moats around the edges of the ice-cover that were initially 1 m wide and continued to widen until ice-off. There was also no snow on the ice and the snow on the surrounding land had also been melting and running into lake overland and through streams. In 2014, there were no moats around the ice which was completely covered in snow and slush. The surrounding area was also still covered in snow. This small difference in duration before ice-off allowed for a significant change in the forcing mechanism of the anomalies. Similar findings were made by *Salonen et al.* (2014) where the small differences in water temperature near the end of the ice cover period have great effects on lake hydrodynamics and the difference in snow and ice conditions can lead to interannual circulation differences. *Rizk et al.* (2014) also observed variation in the direction of rotating density anomalies between years in Lake Pääjärvi which was attributed to the variation in the initial winter stratification which was not measured in either the 2013 or 2014 studies of Lake Kilpisjärvi.

Chapter 5

Conclusion

This work presents analysis (chapter 2) and results (chapter 3) of observations collected in two field seasons near the end of the ice-covered period at Lake Kilpisjärvi. The two field seasons show two different and significant basin-scale circulation patterns beneath the ice. These observations are important because significant basin-scale circulation during the ice-covered period in lakes has not been extensively documented or analyzed. The 2013 observations, presented in section 2.2.1, are also very unique because very few observations have been made directly prior to ice-off which was observed that field campaign.

In 2013, a high-pressure horizontal density anomaly was observed near the centre of the lake. This anomaly had vertically paired rotating circulations in the upper and lower regions of the lake. ADCP measurements show that the level of no-motion was near the bottom boundary of the lake and not at the surface where it as initially assumed to occur. The density distribution was used to estimate the azimuthal velocities which were found to have maximum cyclonic and anti-cyclonic values of 0.03 and 0.02 m s^{-1}. The anomaly was estimated to have $R_{ri} \sim 160$ m, with $R_o \sim 0.2$. It is hypothesized that this circulation is driven by heat flux at the shorelines from incoming streams and, to a lesser extent, the warming of the moats surrounding the ice-cover. This caused a density flow down the slopes to the centre of the lake where the flow converges. From continuity, this flow was balanced with a shoreward flow beneath the ice surface. These flows were modified by the earth's rotation which results in the rotational circulation.

In 2014, a low-pressure horizontal density anomaly was observed near the centre of the lake. This anomaly had vertically paired rotating circulations in the upper and lower regions of the lake. The level of no-motion was estimated to be 10 m below the surface where the circulation transitioned from anti-cyclonic to cyclonic. The density distribution was used to estimate the azimuthal velocities which were found to have maximum cyclonic and anti-cyclonic values of 0.006 and 0.003 m s^{-1}. The anomaly was estimated to have $R_{ri} \sim 240$ m, with $R_o \sim 0.12$. It is hypothesized that this circulation was driven by sediment release of heat to the overlying water causing a tilt in the isopycnals near the shores of the lake that caused an inward pressure force that was balanced by the Coriolis force and, to a lesser extent, the centripetal acceleration force. This is similar to expected results for under-ice circulation.

It is hypothesized that the reason that the observations were different between years was due to the duration between the observation period and ice-off. The 2014 observations were collected 12 days prior to ice-off, and the ice and snow conditions were similar to the conditions during the bulk of winter. The 2013 observations were made directly prior to ice-off, which allowed the snow cover to melt (thus not insulating the lake) and warm inflows to enter the lake. This short period of time allowed for large differences that created significantly different circulation patterns. It was found that for the small horizontal density differences measured under-ice during the 2013 and 2014 studies, the choice of geostrophic or cyclogeostrophic balance does not greatly affect the resulting azimuthal velocities.

Thermal and circulation patterns under-ice are related; however, this relation is not fully understood. These thermal distribution observations and their associated estimated circulation patterns, paired with the ADCP observations of velocity will help to better understand the relationship between thermal patterns and water circulation under ice in lakes.

Bibliography

Akitomo, K., M. Kurogi, and M. Kumagai (2004), Numerical study of a thermally induced gyre system in Lake Biwa, *Limnology*, *5*, 103–114.

Arst, H., A. Erm, M. Leppäranta, and A. Reinart (2006), Radiative characterists of ice-covered fresh- and brackish-water bodies, *Proceedings of the Estonian Academy of Sciences, Geology*, *55*(1), 3–23.

Bengtsson, L. (1986), Dispersion in ice-covered lakes, *Nordic Hydrology*, *17*, 151–170.

Bengtsson, L. (1996), Mixing in ice-covered lakes, *Hydrobiologia*, *322*, 91–97.

Bengtsson, L., and T. Svensson (1996), Thermal regime of ice covered Swedish lakes, *Nordic Hydrology*, *27*, 39–56.

Bengtsson, L., J. Malm, A. Terzhevik, M. Petrov, P. Boyarinov, A. Glinsky, and N. Palshin (1996), Field investigation of winter thermo- and hydrodynamics in a small Karelian lake, *Limnology and Oceanography*, *41*(7), 1502–1513.

Cushman-Roisin, B. (1994), *Introduction to geophysical fluid dynamics*, Prentice Hall, Engelwood Cliffs, N.J.

Ellis, C. R., H. G. Stefan, and R. Gu (1991), Water temperature dynamics and heat transfer beneath the ice cover of a lake, *Limnology and Oceanography*, *36*(2), 324–335.

Emery, K. O., and G. T. Csanady (1973), Surface circulation of lakes and nearly land-locked seas, *Proceedings of the National Academy of Sciences of the United States of America*, *70*(1), 93–97.

Forrest, A. L., B. E. Laval, R. Pieters, and D. S. S. Lim (2013), A cyclonic gyre in an ice-covered lake, *Limnology and Oceanography*, *58*(1), 363–375.

Gill, A. E. (1982), *Atmosphere-Ocean dynamics*, *International Geophysics Series*, vol. 30, Academic Press, Inc.

Gordon, A., W. Grace, P. Schwerdtfeger, and R. Byron-Scott (1998), *Dynamic meteorology: a basic course*, Arnold, London; New York.

Greenspan, H. P. (1968), *The theory of rotating fluids*, Cambridge monographs on mechanics and applied mathematics, Cambridge University Press.

Holton, J. R. (2004), *An introduction to dynamic meteorology*, *International Geophysics Series*, vol. 88, fourth ed., Elsevier.

Huttula, T., M. Pulkkanen, B. Arkhipov, M. Leppäranta, V. Solbakov, S. Kunio, and K. Salonen (2010), Modelling circulation in an ice-covered lake, *Estonian Journal of Earth Sciences*, *59*(4), 298–309.

Kirillin, G., C. Engelhardt, and S. Golosov (2008), A mesoscale vortex in a small stratified lake, *Environmental Fluid Mechanics*, *8*(4), 349–366.

Kirillin, G., M. Leppäranta, A. Terzhevik, N. Granin, J. Bernhardt, C. Engelhardt, T. Efremova, S. Golosov, N. Palshin, P. Sherstyankin, G. Zdorovennova, and R. Zdorovennov (2012), Physics of seasonally ice-covered lakes: a review, *Aquatic Sciences*, *74*, 659–682.

Kirillin, G., A. L. Forrest, K. E. Graves, A. Fischer, C. Engelhardt, and B. E. Laval (2015), Axisymmetric circulation driven by marginal heating in ice-covered lakes, *Geophysical Research Letters*, *(in Revisions)*.

Kundu, P. K., and I. M. Cohen (2004), *Fluid mechanics*, third ed., Elsevier Academic Press.

Leppäranta, M., K. Shirasawa, and T. Takatsuka (2012), Ice season on Lake Kilpisjärvi in Arctic tundra, *Proceedings of the 21st International Association for Hydro-Environment Engineering and Research International Symposium on Ice*, (21).

Likens, G. E., and R. A. Ragotzkie (1966), Rotary circulation of water in an ice-covered lake, *Verhandlungen des Internationalen Verin Limnologie*, *16*(1), 126–133.

Malm, J. (1998), Bottom buoyancy layer in an ice-covered lake, *Water Resources Research*, *34*(11), 2981–2993.

McDougall, T., and P. Barker (2011), *Getting started with TEOS-10 and the Gibbs Seawater (GSW) Oceanographic toolbox*, SCOR/IAPSO WG127, ISBN 978-0-646-55621-5.

Mortimer, C., and F. Mackereth (1958), Convection and its consequences in ice-covered lakes, *Verhandlungen des Internationalen Verin Limnologie*, *13*, 923–932.

Pedlosky, J. (1987), *Geophysical fluid dynamics*, 2 ed., Springer-Verlag, New York.

Renno, N., and H. B. Bluestein (2001), A simple theory for waterspouts, *Journal of Atmospheric Sciences*, *58* (8), 927–932.

Rhines, P. (1998), Circulation, convection and mixing in rotating stratified basins with sloping topography, in *Physical Processes in lakes and oceans*, *Coastal and Estuarine Studies*, vol. 54, edited by J. Imberger, American Geophysical Union.

Rizk, W., G. Kirillin, and M. Leppäranta (2012), Field investigatin of the geostrophic motions in the ice-covered Lake Pääjärvi, *Proceedings of the 21st International Association for Hydro-Environment Engineering and Research International Symposium on Ice*, pp. 1190–1200.

Rizk, W., G. Kirillin, and M. Leppäranta (2014), Basin-scale circulation and heat fluxes in ice-covered lakes, *Limnology and Oceanography*, *59* (2), 445–464.

Salonen, K., M. Pulkkanen, P. Salmi, and R. W. Griffiths (2014), Interannual variability of circulation under spring ice in a boreal lake, *Limnology and Oceanography*, *59* (6), 2121–2132.

Stommel, H., and D. Moore (1989), *An introduction to the Coriolis force*, Columbia University Press, New York.

Timmermans, M.-L., J. Toole, A. Proshutinsky, R. Krishfield, and A. Plueddemann (2008), Eddies in the Canada Basin, Arctic Ocean, observed from ice-tethered profilers, *Journal of Physical Oceanography*, *38*(1), 133–145.

Vincent, W. F., and J. Laybourn-Parry (Eds.) (2008), *Polar lakes and rivers: limnology of Arctic and Antarctic aquatic ecosystems*, Oxford University Press, New York.

Welch, H. E., and M. A. Bergmann (1985), Water circulation in small arctic lakes in winter, *Canadian Journal of Fisheries and Aquatic Sciences*, *42*, 506–520.

Welch, P. S. (1952), *Limnology*, McGraw-Hill, New York.

Wetzel, R. G. (1975), *Limnology*, W. B. Saunders Company, Philadelphia, London, Toronto.

Yang, Y., B. Cheng, E. Kourzeneva, T. Semmler, L. Rontu, M. Leppäranta, K. Shirasawa, and Z. Li (2013), Modelling experiments on air-snow-ice interactions over Kilpisjärvi, a lake in northern Finland, *Boreal Environment Research*, *18*, 341–358.

Zdorovennova, G. E. (2009), Spatial and temporal variations of the water-sediment thermal structures in shallow ice-covered Lake Vendyurskoe (northwestern Russia), *Aquatic Ecology*, *43*, 629–639.

Appendix A

Water Sample Results

Water samples were collected on 2 June 2013 and were analyzed at the University of British Columbia Civil Engineering Department. These results were used for an equation of state to determine the water density from the temperature and specific conductance.

Table A.1: Water sample results

Constituent	Amount [mg L^{-1}]
Phosphate (P04)	<0.02
Calccium (Ca)	2.187
Potassium (K)	0.305
Magnesium (Mg)	0.443
Sodium (Na)	0.955
Strontium (Sr)	0.008
Zinc (Zn)	0.054
Sulfur (S)	1.021
Silicon (Si)	0.552
Silver (Ag)	0.004
Aluminum (Al)	0.004
Barium (Ba)	0.022